FULL-WAVEFORM INVERSION OF GPR DATA FROM THE THUR RIVER AQUIFER

Published in *Near Surface Geophysics*:

Klotzsche, A., van der Kruk, J., Meles, G. A., Doetsch, J., Maurer, H., and Linde, N., 2010, Full-waveform inversion of cross-hole ground-penetrating radar data to characterize a gravel aquifer close to the Thur River, Switzerland: *Near Surface Geophysics*, **8**, 635-649.

ABSTRACT

Crosshole radar tomography is a useful tool for mapping shallow subsurface electrical properties viz. dielectric permittivity and electrical conductivity. Common practice is to invert crosshole radar data with ray-based tomographic algorithms using first arrival traveltimes and first cycle amplitudes. However, the resolution of conventional standard ray-based inversion schemes for crosshole ground penetrating radar (GPR) is limited because only a fraction of the information contained in the radar data is used. The resolution can be improved significantly by using a full-waveform inversion that considers the entire waveform, or significant parts thereof. A recently developed 2-D time-domain vectorial full-waveform crosshole radar inversion code has been modified in the present study by allowing optimized acquisition setups that reduce the acquisition time and computational costs significantly. This is achieved by minimizing the number of transmitter points and maximizing the number of receiver positions. The improved algorithm was employed to invert crosshole GPR data acquired within a gravel aquifer (4 - 10 m depth) in the Thur valley, Switzerland. The simulated traces of the final model obtained by the full-waveform inversion fit the observed traces very well in the lower part of the section and reasonably well in the upper part of the section. Compared to the ray-based inversion, the results from the full-waveform inversion show significantly higher resolution images. At either side, 2.5 m distance away from the crosshole plane, borehole logs were acquired. There is a good correspondence between the conductivity tomograms and the Natural Gamma logs at the boundary of the gravel layer and the underlying lacustrine clay deposits. Using existing petrophysical models, the inversion results and Neutron-Neutron logs are converted to porosity. Without any additional calibration, the values obtained for the converted Neutron-Neutron logs and permittivity results are very close and similar vertical variations can be observed. The full-waveform inversion provides in both cases additional information about the subsurface. Due to the presence of the water table, and associated refracted/reflected waves, the upper traces are not well fitted and the upper 2 m in the permittivity and conductivity tomograms are not reliably reconstructed because the unsaturated zone is not incorporated into the inversion domain.

A.1 INTRODUCTION

Crosshole radar tomography is a useful tool for mapping shallow subsurface electrical properties, such as dielectric permittivity (ε) and electrical conductivity (σ), in connection with assorted geological, hydrological and engineering investigations. These parameters are

closely linked with important hydrogeological parameters like salinity, water content, porosity and pore structure, clay content, and lithological variations [*Archie*, 1942; *Topp et al.*, 1980; *al Hagrey and Müller*, 2000; *Barrash and Clemo*, 2002; *Garambois et al.*, 2002; *Linde et al.*, 2006a; *Turesson*, 2006]. Crosshole radar surveying entails the generation of high-frequency electromagnetic pulses from a dipole-type antenna which is sequentially positioned at a number of locations along a borehole. The resulting transmitted and scattered waves are detected (and subsequently recorded) by means of a dipole antenna which is progressively moved to a number of discrete locations in a second borehole. The center frequency of most borehole antennas for GPR lies in the range 20-250 MHz (dominant wavelengths of 5-0.4 m) for common geologic materials.

A number of studies have estimated hydrogeological parameters by inverting crosshole ground penetrating radar (GPR) data using ray-based inversion schemes, similar to that described by *Holliger et al.* [2001]. For example, *Tronicke et al.* [2002] examined the integration of surface GPR and crosshole radar tomography on braided stream deposits while *Binley et al.* [2002b; 2002a] and *Winship et al.* [2006] used crosshole GPR to monitor moisture content changes arising from tracer experiments. *Linde et al.* [2006a] were able to improve hydrogeological characterization by using a joint inversion of crosshole electrical resistance and (GPR) traveltime data. *Looms et al.* [2008] monitored unsaturated flow and transport by using cross-borehole GPR and electrical resistance tomography (ERT). These traditional tomographic inversions of crosshole GPR data use separate inversions of traveltimes and maximum first cycle amplitudes based on ray theory and provide velocity and attenuation images of the subsurface that can be transformed into electromagnetic permittivity and electrical conductivity. Radar tomography based on ray theory provides only limited resolution and can account for just a small fraction of the information in the traces, such that small targets (smaller than the dominant wavelength) cannot be satisfactorily detected and imaged. By contrast, full-waveform inversion not only takes into account the arrival-times and first cycle amplitudes, but considers the entire waveforms (or at least the first few cycles) which include secondary events like forward scattered and refracted waves. Therefore, full-waveform inversions provide higher resolution images and can thus yield more detailed information for a wide range of applications.

Waveform-based inversion schemes were first developed in seismic exploration subject to the acoustic (P-wave only) approximation [*Tarantola*, 1984a; b; 1986] and later modified for elastic (P + S) wave propagation [*Mora*, 1987]. Following these early developments, several

inversion methods were developed and applied to seismic data for surface and/or borehole measurements. The methods have been adapted to the acoustic-, elastic-, viscoelastic-, and anisotropic-wave equations in both the time and frequency domain, using finite-difference and finite-element approaches to solve the forward problem i.e. to generate the synthetic seismograms [e.g., *Bing and Greenhalgh*, 1998a; b; *Pratt*, 1999; *Pratt and Shipp*, 1999; *Zhou and Greenhalgh*, 2003; *Watanabe et al.*, 2004]. Full-waveform seismic inversion is extensively discussed in the November 2008 issue of the journal Geophysical Prospecting and contains numerous other references. Comparable efforts for the full-waveform inversion of GPR data have been limited to just a few papers [*Ernst*, 2007; *Ernst et al.*, 2007b; *Ernst et al.*, 2007a; *Kuroda et al.*, 2007; *Meles et al.*, 2010]. *Ernst et al.* [2007a] developed a full-waveform scalar inversion scheme for electromagnetic waves for crosshole GPR data based on the 2-D finite difference time domain solution of Maxwell's Equations using generalized perfectly matched layers (GPML) to reduce artifacts from reflections at the boundaries and edges of the model space. This scheme was tested on synthetic and observed crosshole data [*Ernst et al.*, 2007b]. It was shown that this algorithm provides higher resolution permittivity and conductivity images of the subsurface than conventional ray-based techniques. Similar to *Ernst et al.* [2007b], *Kuroda et al.* [2007] applied a full-waveform inversion algorithm to synthetic crosshole radar data. Meles *et al.* [2010] improved the method of *Ernst et al.* [2007b; 2007a] by including the vector properties of the electric field, which enabled extension of the algorithm to incorporate surface-to-borehole measurements, in addition to crosshole measurements. Furthermore, the permittivity and conductivity parameters were simultaneously updated, which proved to be superior to the sequential (cascaded) update approach of *Ernst et al.* [2007a].

In this work we apply the approach described in *Meles et al.* [2010] to invert a crosshole GPR data set acquired within a gravel aquifer in northern Switzerland (Chapter 2). First, we give an overview of the full-waveform inversion algorithm. Then, we discuss the borehole setup and measurements, followed by our data analysis procedures. Finally, the reliability of the inversion results is investigated by comparisons with borehole logging data.

A.2 FULL-WAVEFORM INVERSION METHODOLOGY

The workflow of the full-waveform inversion scheme which uses a simultaneous updating of permittivity and conductivity is shown in Figure C1. First, we describe the pre-processing

followed by the source wavelet estimation. Then we discuss the inversion algorithm and implementation details.

A.2.1 Pre-Processing

Initially, the data are band-pass filtered to remove noise outside the source spectrum (Figure C1, step A). A good initial model is required for the full-waveform inversion algorithm to converge to the global minimum. Otherwise it may get trapped in a local minimum. The starting model is typically obtained by standard ray-based inversion techniques. First-arrival traveltimes and first-cycle amplitude are used for the ray-based inversion to obtain velocity and attenuation tomograms of the subsurface which are then transformed into permittivity and conductivity distributions (Figure C1, step B).

To apply the 2-D-full-waveform inversion algorithm to real data it is necessary to account for the 3-D radiation characteristics of electromagnetic wave propagation. Similar to *Ernst et al.* [2007b] we apply a 3-D to 2-D transformation technique developed by *Bleistein* [1986] to compensate for differences in geometrical spreading and pulse shape (frequency scaling and phase shifting; Figure C1, step C).

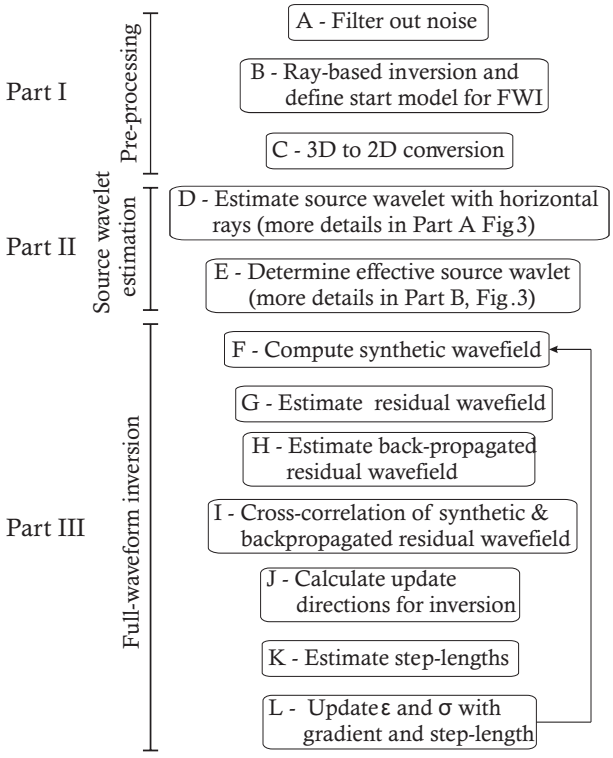

Figure C1. Full-waveform inversion workflow showing the three main parts: pre-processing, source wavelet estimation and full-waveform inversion. The arrow indicates that these steps should be repeated until the misfit between the observed and synthetic data between iterative steps is below 1%.

A.2.2 Source wavelet estimation

The source wavelet estimation (Figure C1, steps D and E) is a critical step in the inversion. Only through obtaining an effective source wavelet is it possible to match the measured waveforms, including any small nuances, which may be present. This wavelet not only reflects the current density pattern of the finite length GPR antenna but also its radiation pattern in a water-filled borehole. The steps in the source wavelet recovery are illustrated in detail in Figure C2 [extended from *Ernst et al.*, 2007b], where the Fourier transformed quantities are indicated by ^. First, an initial source wavelet is estimated (Figure C2, Part A), where only the shape of the wavelet is determined without considering any amplitude information. All traces from a vertical zero offset profile (ZOP), containing only horizontally traveling waves, are normalized and aligned to estimate an average pulse (Figure C2, step 1). By cross-correlating the ZOP traces, data containing erroneous wave shapes due to e.g., interfering reflections are identified and excluded. We know from Maxwell's equations that the electric field is proportional to the time derivative (multiplication with $i\omega$ in the frequency domain) of the current density source wavelet. To obtain the shape of the initial source wavelet we divide the average Fourier transformed pulse (electric field) by $i\omega$ in the frequency domain (Figure C2, step 2).

In Part B (Figure C2) we calculate a corrected wavelet with detailed amplitude and phase characteristics. The forward modeling is done using the Cartesian coordinate, 2-D finite-difference time-domain (FDTD) code of *Ernst et al*. [2007a]. The synthetic radargrams $\mathbf{E}^{\mathrm{syn}}$, for each transmitter-receiver position, are calculated using the model of permittivities and conductivities obtained from the ray-based inversion (indicated by "*ray"*) and the initial source wavelet (Figure C2, step 3 and 4). The radar data can be viewed as the convolution of the source wavelet with the impulse response (Green's function) in the time-domain or as the multiplication of the source spectrum with the Fourier-transformed Green's function. Therefore, an effective source wavelet can be obtained by deconvolving the radar data $\hat{\mathbf{E}}^{\mathrm{obs}}$ with an appropriate Green's function $\hat{\mathbf{G}}$ calculated using the traveltime inversion results as input. This is best done using a least-squares approach in the frequency domain [*Ernst et al.*, 2007b; *Streich and van der Kruk*, 2007b]. The transfer function $\hat{\mathbf{G}}$ is calculated by spectral division of $\hat{\mathbf{E}}^{\mathrm{syn}}$ in the frequency domain with the initial wavelet spectrum $\hat{\mathbf{S}}_{k=0}$ for each separate trace (Figure C2, step 5). Next, we estimate $\hat{\mathbf{S}}_{k=1}$ by dividing the actual observed data $\hat{\mathbf{E}}^{\mathrm{obs}}$ with the transfer function $\hat{\mathbf{G}}$, using all traces in a least squares sense (Figure C2, step 6). Quantities η_{D} and η_{I} are prewhitening factors which are applied to stabilize the solution and

avoid dividing by zero (should there be any notches in the spectrum of **G**). The time-domain source wavelet $S_{k+1}(t)$ is obtained by an inverse Fourier transformation (Figure C2, step 7). Steps 3-7 can be repeated until the source wavelet has converged (Loop 1), where *k* indicates the iteration number. In Part C (Figure C2) a source wavelet refinement can be applied during the full-waveform inversion to improve the wavelet when necessary (Loop 2).

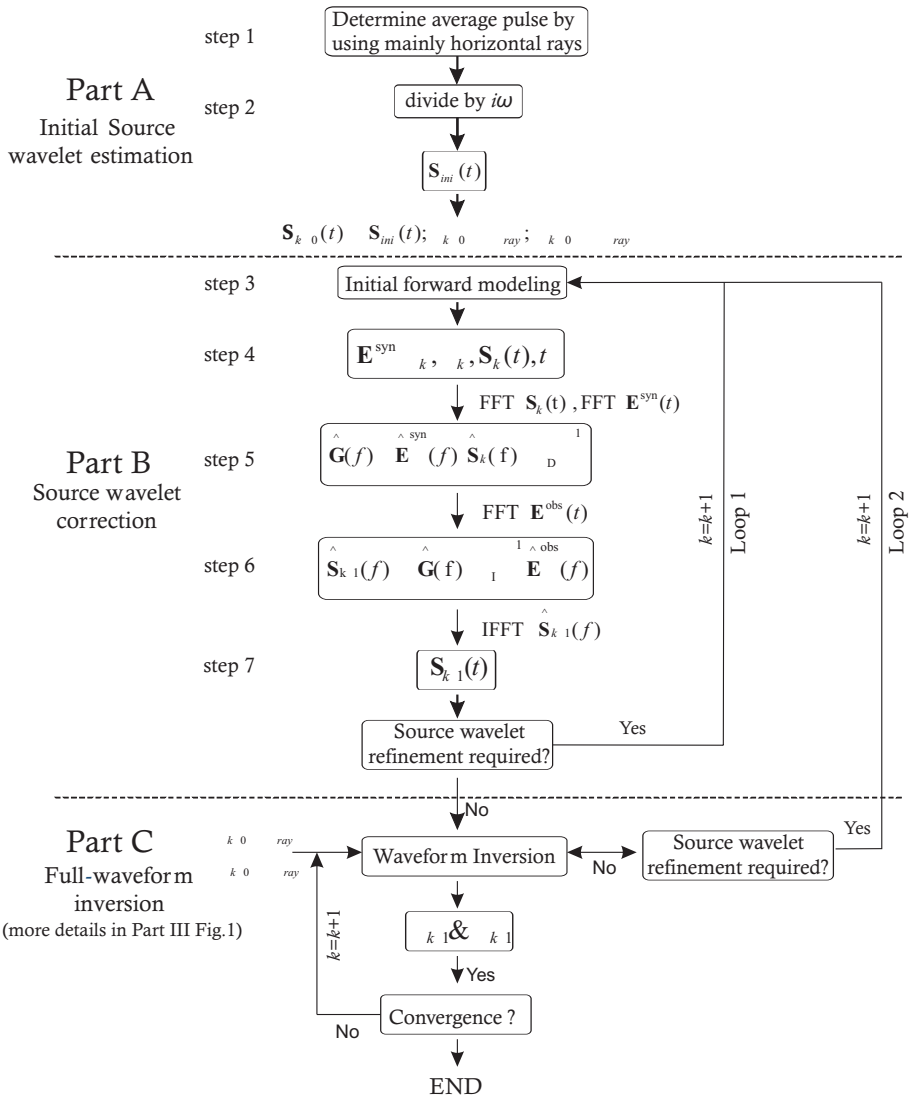

Figure C2. Source wavelet estimation flow consisting of three parts: Part A - initial source wavelet estimation using averaged horizontal rays (steps 1-2), Part B - the source wavelet correction (steps 3-7) with the deconvolution method using all available data (extended from *Ernst et al.* [2007b]) and Part C - source wavelet refinement during the full-waveform inversion. This source wavelet estimation is always carried out before starting the full-waveform inversion (loop 1), and can also be performed after several iterations of the full-waveform inversion (loop 2).

A.2.3 Inversion algorithm

The full-waveform inversion is based on Tarantola's approach [1984a; b; 1986] and uses a gradient-type method (Figure C1, Part III). The cost function (or misfit function) $\mathbf{C}=0.5\left\|\mathbf{E}^{syn}-\mathbf{E}^{obs}\right\|^2$, which is the difference between the simulated ($\mathbf{E}^{syn}$) and observed ($\mathbf{E}^{obs}$) traces, is minimized for all transmitter-receiver combinations within a selected time window. This is achieved by computing the gradient of **C**, which indicates the update direction of the permittivity and conductivity models. Furthermore, individual step lengths need to be determined that indicate the magnitude of the model updates.

To calculate the gradient $\nabla\mathbf{C}$, the forward propagated wavefield $\mathbf{E}^{syn}$ is computed using the estimated source wavelet and the model from the previous inversion iteration (the ray-based inversion model is used for the first iteration). The wavefields are stored in memory for each transmitter and each time step (Figure C1, step F). Then, the residual wavefield is calculated by subtracting the synthetic wavefield from the observed wavefield (Figure C1, step G) and for each transmitter, this residual wavefield is backpropagated from all receivers to the corresponding transmitters (Figure C1, step H). Finally, the gradient at each point **x** is obtained by a zero-lag cross-correlation of the stored values of $\mathbf{E}^{syn}$ with the backpropagated residual wavefield, and by summing over all transmitters and times (Figure C1, step I and J). Constructive interference occurs at positions in space where the true and modeled medium properties deviate, and the gradient indicates how to change the model parameter values to reduce the misfit function.

After estimating the permittivity and conductivity gradients (Figure C1, step J), the step-lengths are calculated (Figure C1, step K). According to *Meles et al.* [2010] individual step-lengths are necessary to simultaneously update the permittivity and conductivity models. Finally, the permittivity ε and conductivity σ at the current iteration are updated with the obtained gradient directions and step lengths (Figure C1, step L). For terminating the inversion loop, we use a stopping criterion of 1% change of the root mean square (RMS) error between the observed and synthetic data between subsequent iterations [*Ernst et al.*, 2007b].

A.2.4 Implementation details

The computational costs of the full-waveform inversion are determined mainly by the FDTD calculations. The full-waveform algorithm requires solving the forward problem four times during each iteration. With the first solution the residual wavefield is calculated, the second solution is required to compute the model update directions (gradients) and two FDTD

calculations are needed for determining the step-lengths. The calculations for each transmitter position are independent from each other. Therefore, the algorithm can be parallelized easily (for each transmitter one slave CPU is required, and one master CPU coordinates the computations). The overhead for the distribution of the computations is about 10% using the MPI system [*Ernst et al.*, 2007b; *Ernst et al.*, 2007a].

During the calculation of the gradient, the forward modeled field $\mathbf{E}^{\mathrm{syn}}$ remains in the computer memory. The required memory M is estimated by

$$M(bytes) = \frac{n_{xf} \cdot n_{zf} \cdot timesamples \cdot 2 \cdot 8}{invfwd^2} \cdot N_{TRN}, \tag{C1}$$

where n_{xf} and n_{zf} are the numbers of the horizontal and vertical forward modeling cells, the value 2 indicates the two components ($\mathbf{E}_x$ and $\mathbf{E}_z$) of the electric field, the 8 indicates the double-precision number representation in bytes of the electric field values and N_{TRN} is the number of transmitters. Due to memory constraints, each inversion cell consists of *invfwd*=3 forward modeling cells in the x and z directions, which is indicated by the square of the factor *invfwd*. For the data set presented in the next section, this requires approx. 2.4 Gbytes. The computation time is

$$T_{comp} = 4 \cdot 1.1 \cdot T_{forward} \cdot N_{iter}, \tag{C2}$$

where $T_{forward}$ is the time for a single FDTD calculation and N_{iter} is the number of iterations (Meles *et al.* 2010). For the calculations, two different computer clusters are used; the JUMP (Research Center Jülich) and the HPC cluster (RWTH Aachen). The computing times on the JUMP and HPC cluster are 0.2 min per iteration (for 51 iterations 12.4 min) and 0.6 min (for 51 iterations 32 min), respectively.

A.3 CASE STUDY: THUR RIVER HYDROGEOPHYSICAL TEST SITE

In this section, we explore the potential and limitations of the ray-based and full-waveform inversion schemes using an experimental data set. First, we describe the field site and the survey geometry. Then, we show the ray-based inversion results, estimate the source wavelet and describe the full-waveform inversion. Finally, we compare the results obtained with geophysical well logs acquired in neighboring boreholes.

A.3.1 Test site

The crosshole GPR data set was acquired in the Thur valley close to Frauenfeld, Switzerland. The Thur valley was initially formed by glaciers during the Pleistocene, which

cut into the older underlying Tertiary bedrock. Today, the valley is filled with lacustrine sediments and the central part of the Thur River is 40 to 45 m wide. On the south side of the Thur River, an overbank was formed with an approximate width of 130 m [*Cirpka et al.*, 2007]. The aquifer comprises a 7 m thick glaciofluvial gravel deposit, which is embedded between a thick sequence of low permeable clays (lacustrine sediments) below and alluvial loam above, which has a thickness of 3 m (Figure C3). Within the framework of the RECORD project [*RECORD*, 2011] four 11.4 cm diameter monitoring wells were installed in 2007 close to the Thur River, where measurements of crosshole GPR, ERT and seismic data have been performed (Chapter 2 and 4, and Appendix B). We consider here only the crosshole GPR data acquired along the south-west plane of the six planes interpreted in Chapter 2.

A.3.2 Measurement setup

A limited number of transmitter positions were used during the data acquisition to minimize acquisition time. To ensure that enough information is captured to reliably invert the data, a much larger number of receiver positions were occupied. The disadvantage of this approach is that ray coverage close to the transmitter borehole is relatively low (see Figure C4a). This is overcome by using a semi-reciprocal transmitter-receiver setup shown in Figure C4b, in which transmitter and receiver boreholes are interchanged. The combination of both data sets results in adequate ray-coverage over the entire domain (Figure C4c). In addition, this setup also reduces the computational costs, as discussed above.

For the GPR measurements, a RAMAC Ground Vision system of Malå Geoscience with 250 MHz antennas was employed. The vertical spacing between the transmitters and receivers are 0.5 m and 0.1 m, respectively. For the purpose of characterizing the aquifer between 4 and 10 m depth, 12 transmitter and 59 receiver positions were chosen in the south and west borehole, respectively (SW setup) and for the semi-reciprocal setup 12 transmitter and 57 receiver positions were chosen in the west and south borehole, respectively (WS-setup, see also Figure C4). In Figure C5a, these setups are shown with the transmitters and receivers indicated by white circles and blue crosses in the boreholes, respectively. Due to the measurement setup, the receiver records rays up to an angle of approximately 50° and all measurements were performed below the water table, which is located at approximately 4 m depth. The zone above the water table is neither included in the measurements nor in the inversion volume, so any recorded signals which have refracted/reflected from this horizon are not accommodated in the forward modeling and inversion.

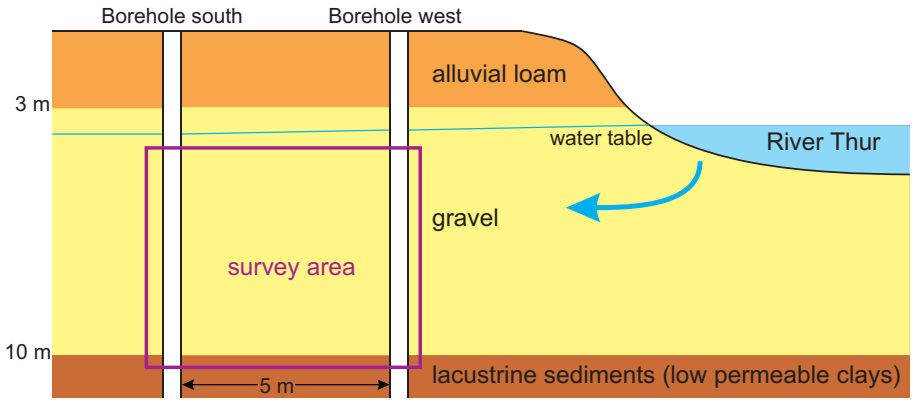

Figure C3. Simplified geological representation of the experimental area, showing a three-layer structure: alluvial loam, gravel, lacustrine (clay) sediments (from top to bottom); with boreholes close to the Thur River. The water table is approximately at 4 m depth.

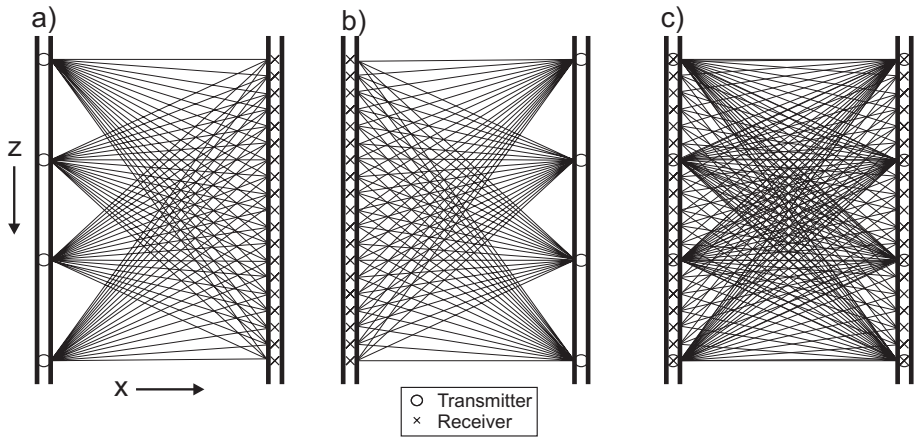

Figure C4. Schematic of the measurement setup employed that requires significantly less transmitter than receiver positions, but has low ray-coverage in the transmitter borehole. Semi-reciprocal measurements, in which transmitter and receiver boreholes are interchanged, are indicated in (a) and (b). The combination of these measurements, shown in (c), improves the ray-coverage compared to the individual setups.

A.3.3 Estimation of the initial model with ray-based inversion scheme

The first step in the processing sequence consists of picking the first-arrival traveltimes and the first cycle amplitudes of the measured data. The ray-based inversion is performed by minimizing the misfit between the picked traveltimes and the first cycle amplitudes of the measured and calculated data for a given fixed model regularization that includes both damping and smoothness constraints [*Holliger et al.*, 2001; *Maurer and Musil*, 2004]. The obtained velocity and attenuation tomograms are transformed into permittivity and conductivity images (Figure C5a and b). For convenience, we use the relative permittivity $\varepsilon_r=\varepsilon/\varepsilon_0$ (or dielectric constant), where ε_0 is the free space permittivity. Both permittivity and

conductivity images reveal roughly three zones. A zone of higher permittivity and higher electrical conductivity is found in the top 4 m to 5.5 m, followed by lower permittivity and lower conductivity values between 5.5 m to 8 m. The bottom part exhibits intermediate values for both parameters. Neglecting the critically refracted waves results in a low ray density in the uppermost part of the tomographic plane. In addition, the high permittivities (low velocities) cause most of the rays to avoid the upper part (Figure C5c). Therefore, small-scale features found within this zone should be viewed with caution and not be over-interpreted.

A.3.4 Source wavelet estimation

Before the source wavelet estimation can be performed, it is necessary to apply a 3-D to 2-D conversion to transform the 3-D field data to make them comparable with the 2-D modeling data i.e. synthetic traces [*Ernst et al.*, 2007b]. These transformed data are then used in all the following processing steps, as well as the full-waveform inversion.

Initial source wavelet estimation

Following the scheme outlined in Figure C2 Part A, the traces of the upper and lower neighboring receivers of the ZOP data are at first averaged. Then the similarity of these waveforms obtained for each transmitter is investigated using a cross-correlation procedure for the horizontally traveling waves. Waveforms having relative cross-correlation values below 0.8, which indicate significantly differences, are discarded. Waveforms of SW-transmitters 1, 2 and 12 and WS-transmitters 13, 14, 23 and 24 were excluded.

In the next step, all traces are aligned to the largest pulse minimum, which results in a better alignment than using the largest maximum of the pulses [as used by *Ernst*, 2007], and integrated (see also Figure C2). A bandpass filter is applied in the frequency domain to remove frequencies below 40 MHz and above 150 MHz. The tapered and normalized initial wavelet is plotted in blue in Figure C6. Note that only the shape is estimated and the amplitude scale is not considered.

The initial source wavelet is employed for modeling the radargrams using the ε and σ distributions obtained from the ray-based inversion. In Figure C7, the experimental data for the SW-setup are compared with the synthetic data. The amplitudes for each trace are normalized to the maximum to enable a better comparison of the data. Negative and positive amplitudes are indicated by the blue and red color in the image, respectively. The images show a similar trend for both data sets. However a timeshift of about 3 ns is apparent, especially in Figures C8a, b and c, where the observed and synthetic data are compared in

more detail and normalized wiggle plots are shown for the selected transmitter positions 2, 7 and 11, respectively, of the SW-setup with their respective receivers. The red and blue traces show the observed and synthetic traces, respectively. Only traces containing waves that mainly travelled horizontal paths show a good fit with the synthetic data (green ellipses). High-angle data contain significant time shifts and transmitters close to the water table have a significant misfit, which is probably due to reflections being present in the top 20 traces from transmitters 2 and 7. Similar results were obtained for the WS-setup.

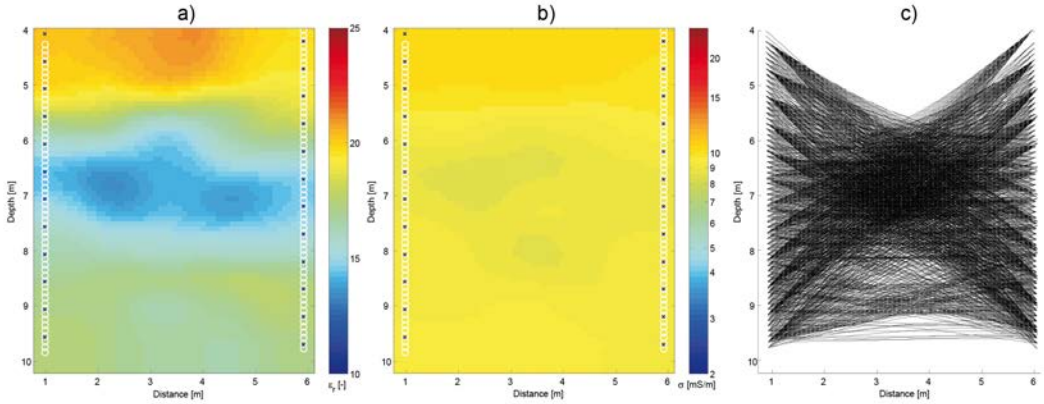

Figure C5. Ray-based inversion results that are used as the initial model for the full-waveform inversion. (a) The distribution of permittivity and (b) conductivity; transmitter and receiver positions are indicated with crosses and circles, respectively. (c) The ray-coverage based on the traveltime inversion.

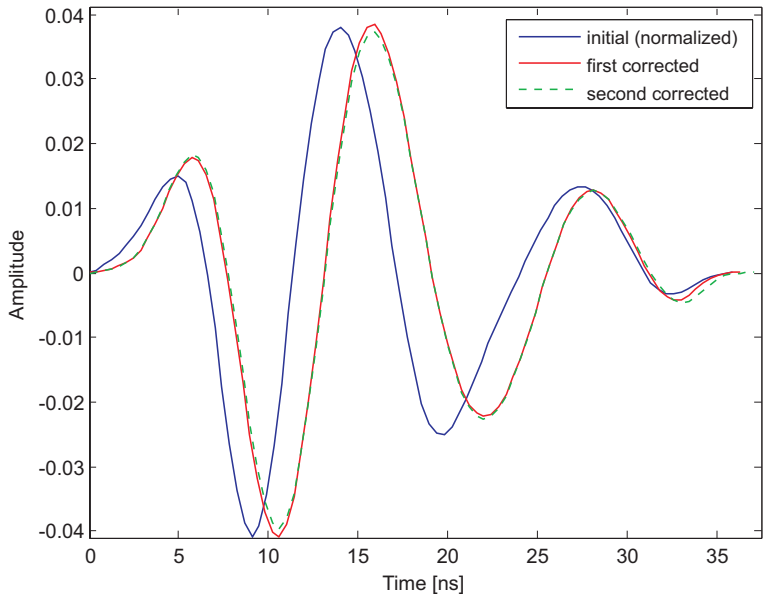

Figure C6. Wavelets for different processing steps: the initial wavelet which is normalized to the maximum amplitude of the first corrected wavelet (blue), first corrected wavelet (red), and the second corrected wavelet (green).

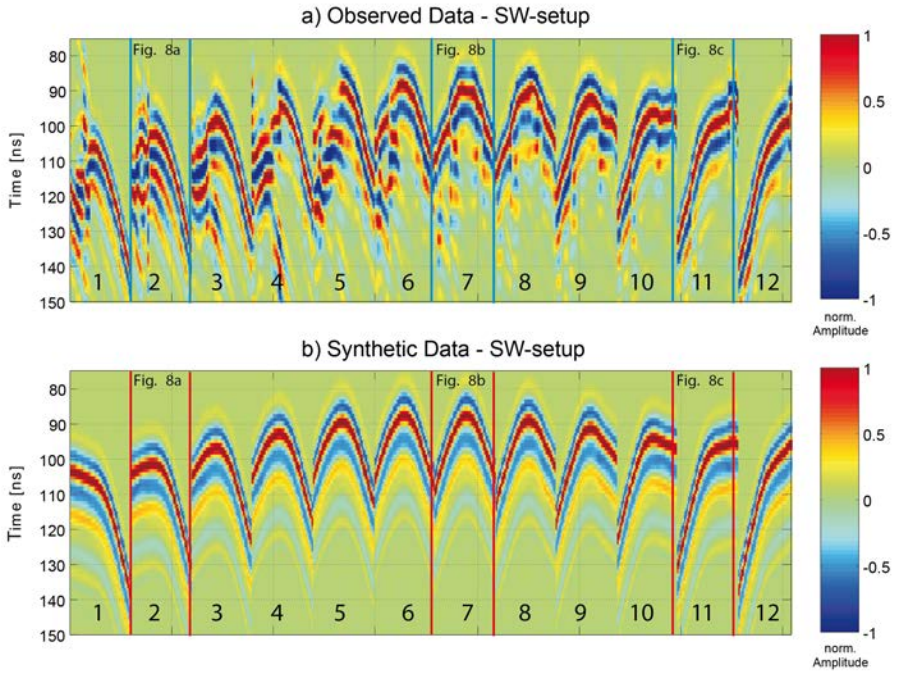

Figure C7. Comparison after one forward modeling run of the observed (a) and synthetic (b) data for the SW-setup (amplitudes normalized to their maximum). The numbers indicate the transmitter positions. Wiggle trace plots for observed and synthetic data for transmitters 2, 7 and 11 are shown in Figure C8a, b and c, respectively.

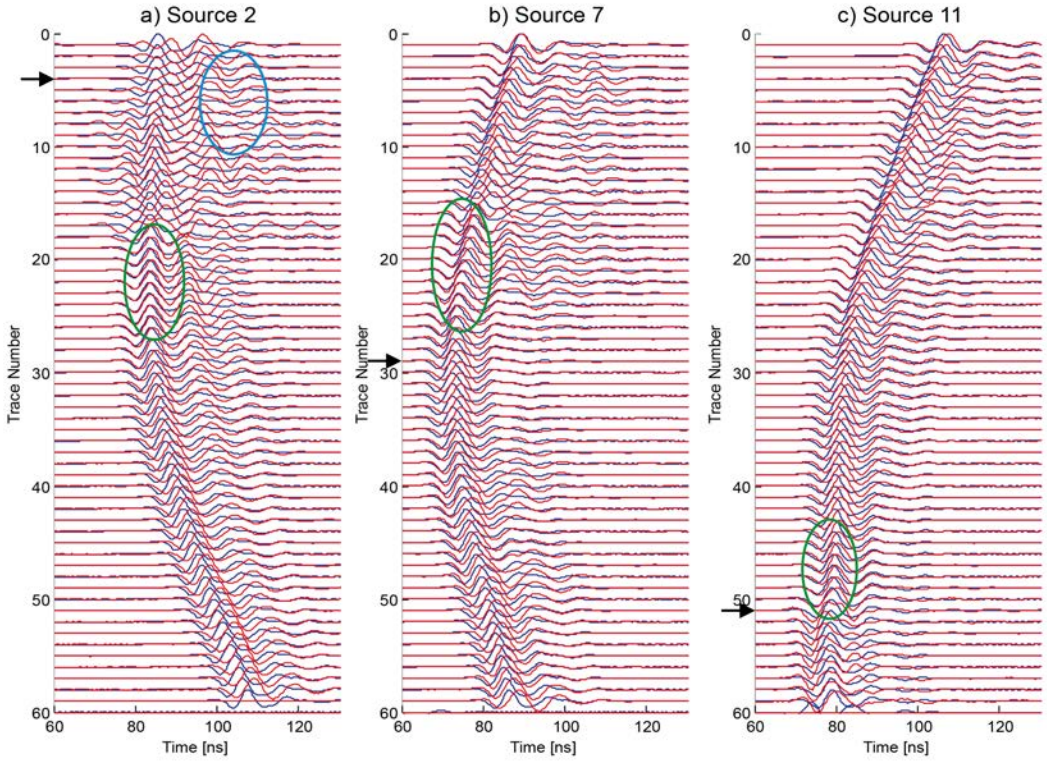

Figure C8. Comparison of normalized observed (red) and synthetic (blue) traces after the first forward modeling run for the transmitter gathers at positions (a) 2, (b) 7 and (c) 11. The green ellipses indicate the areas of best fit between the traces. The arrows at trace number (a) 4, (b) 29 and (c) 51 indicate the locations of transmitters 2, 7 and 11, respectively.

Source wavelet correction and refinement

In the next step, the source wavelet is corrected according to Figure C2, Part B. In contrast to the initial source wavelet estimation, where only horizontal rays are considered, we now use all traces to estimate the corrected wavelet. The amplitude and phase spectra of the wavelets are shown in Figures C9a and b, respectively. The blue, red and dashed black lines show the initial wavelet, the wavelet after the deconvolution and the final corrected wavelet, respectively. The frequency band (corner frequencies) of the bandpass filter applied during pre-processing is shown by the vertical dotted green lines. Within the bandpass there is a good match of the amplitude spectrum (Figure C9a), whereas the phase spectrum still shows a significant shift. The resulting wavelet, marked as the red curve in Figure C6, shows a compensation of the earlier observed timeshift between the observed and synthetic data in Figures C7 and C8. This shift probably arises because the first estimation of the wavelet is based only on a limited number of averaged direct waves, and no exact time zero is known and only the general form is obtained. Note that the amplitude of the corrected wavelet is now also determined, whereas the initial wavelet (blue line in Figure C6) is normalized to the maximum of the first corrected wavelet to allow a comparison of the shape with the corrected wavelet (corrected wavelet amplitude is about 1/25 of the initial wavelet amplitude).

To investigate and refine the shift and the amplitude, one more correction of the source wavelet is applied. The same steps and parameters are used in the second correction cycle (green wavelet in Figure C6). The wavelet did not change much and was found to be stable, suggesting that the shape and the amplitude are properly obtained. Figure C10 shows a comparison of the observed and synthetic data for the same transmitter positions as in Figure C8. The events show similar trends and no normalization is applied. It is obvious that the data fit improves and that both data sets are more comparable. The observed and synthetic traces have now the same first-arrival times, and the amplitudes for the traces correspond well when the transmitter and receiver positions are aligned sub-horizontally (see green ellipses). The time shift of 3 ns, which was observed after the first forward modeling, is absent. However, with increasing angle from the transmitter, the fit to the observed amplitudes becomes progressively worse.

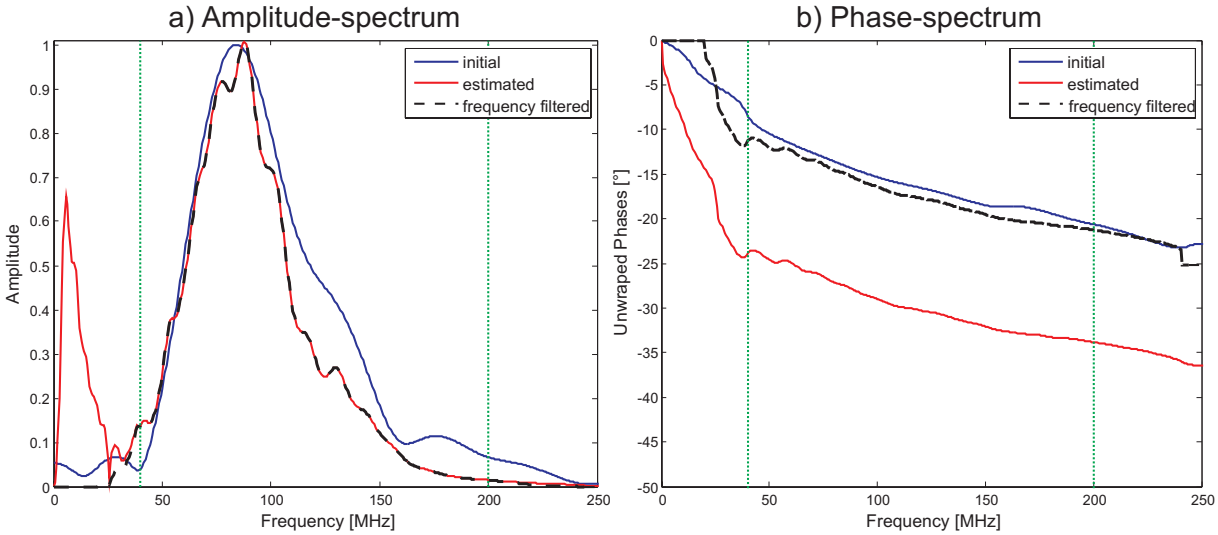

Figure C9. (a) Amplitude and (b) phase spectra of the initial source wavelet (blue), the estimated wavelet (red) and the frequency filtered wavelet (dashed black). A bandpass frequency filter is applied, having corner frequencies indicated by the green dotted lines.

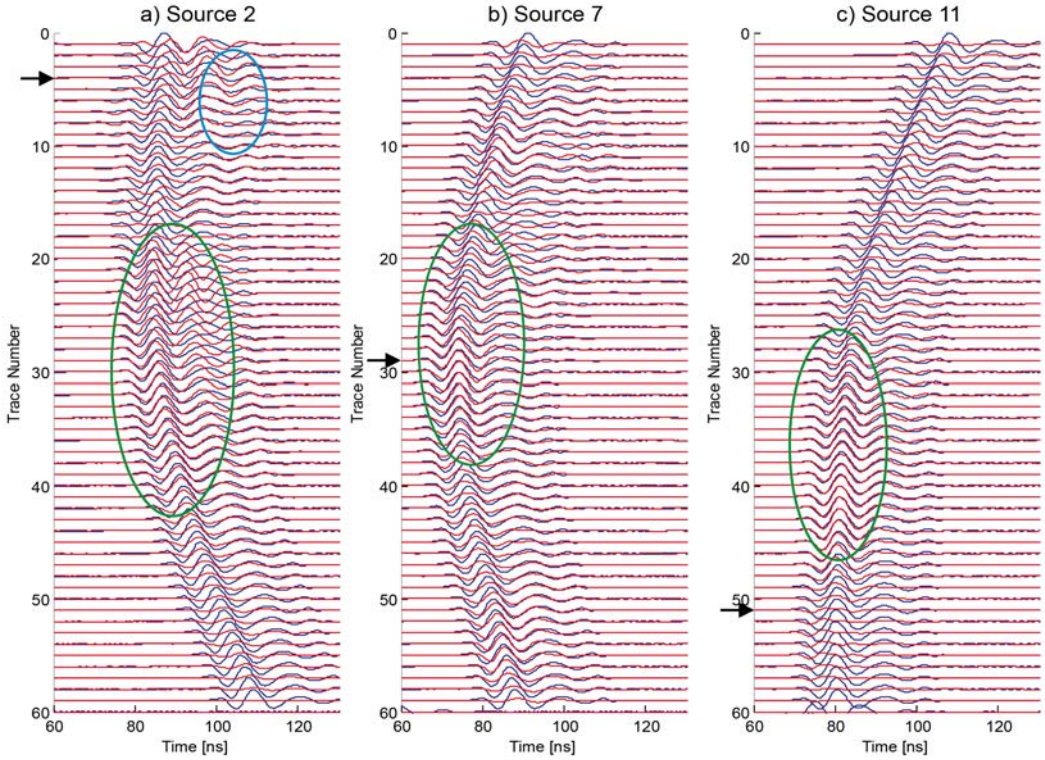

Figure C10. Comparison of non-normalized observed (red) and synthetic (blue) traces after the second forward modeling run for the measurements of the transmitter positions (a) 2, (b) 7 and (c) 11. The green ellipses indicate where the best fit between the traces.

A.3.5 Full-waveform permittivity and conductivity inversions

The Full-waveform inversion (Figure C1 Part III) begins by computing a synthetic wavefield using the ray-based results, shown for the permittivity in Figure C11a (iteration 0). Figures C11b, c and d show the permittivity tomograms obtained for iterations 10, 20 and 35, respectively. In the upper 2 meters the image changes between iteration 0 and 20, and regions with a higher permittivity become visible. Also, over the depth range 5.5 m to 10 m more structures and layering become evident. After iteration 20, the tomograms remain relatively constant until the final solution (iteration 35) in Figure C11d. The final permittivity image shows much more details than the ray-based inversion result. The aquifer area between depths of 4 m and 5.5 m contains thin layers having very high contrasts. Instead of the more or less homogenous middle layer obtained from the traveltime inversion, the area between 6 m and 7.5 m depth contains two areas of relatively low permittivity. Below this area four intermediate and two lower permittivity zones are resolved.

Figure C12a shows the initial conductivity model (logarithmic scale) obtained from the ray-based inversion (iteration 0) using the first cycle amplitudes. The conductivity tomograms for iterations 10, 20 and 35 are shown in Figure C12b, c and d, respectively. In contrast to the permittivity tomograms, where small-scale features become visible in the earlier iterations, the conductivity tomograms remain relatively smooth during the first 20 iterations whereas finer details only occur for the later iterations. The reason is that the permittivity inversion model must first converge to ensure matching the phases between the synthetic and real data. Otherwise, the waveforms are not time-aligned and the amplitudes cannot be effectively optimized. A kinematic shift of more than one quarter of a pulse period precludes a satisfactory dynamic inversion. The final conductivity tomogram shows much more detail than the ray-based model (iteration 0). A very pronounced higher conductivity zone is imaged at a depth below 9.5 m (black dashed line in Figure C12d), which was not obtained with the ray-based inversion results (Figure C12a).

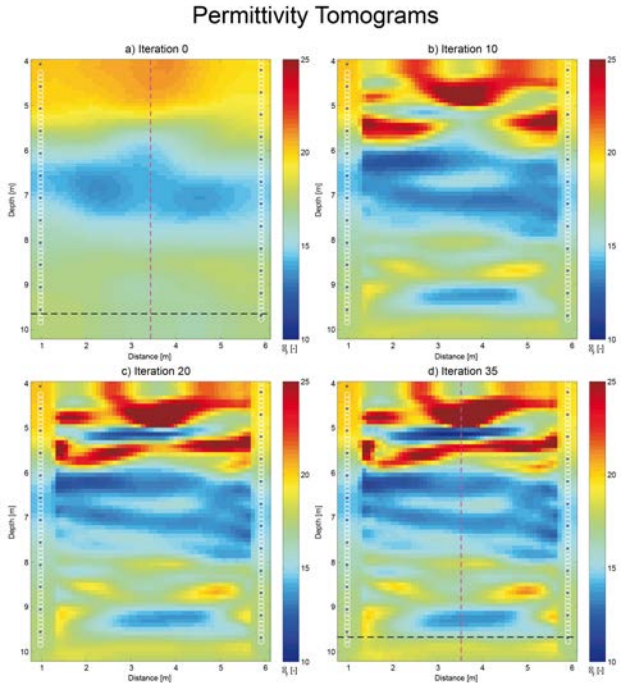

Figure C11. Relative permittivity tomograms for different iteration steps from (a) initial model of the full-waveform inversion obtained from the ray-based inversion, (b), (c) and (d) show the models obtained at iterations 10, 20 and 35, respectively. The dashed black line refers to Figure C15a, where a comparison of Neutron-Neutron logging data is presented. The violet dashed line indicates the position of the logging boreholes (2.5 m away).

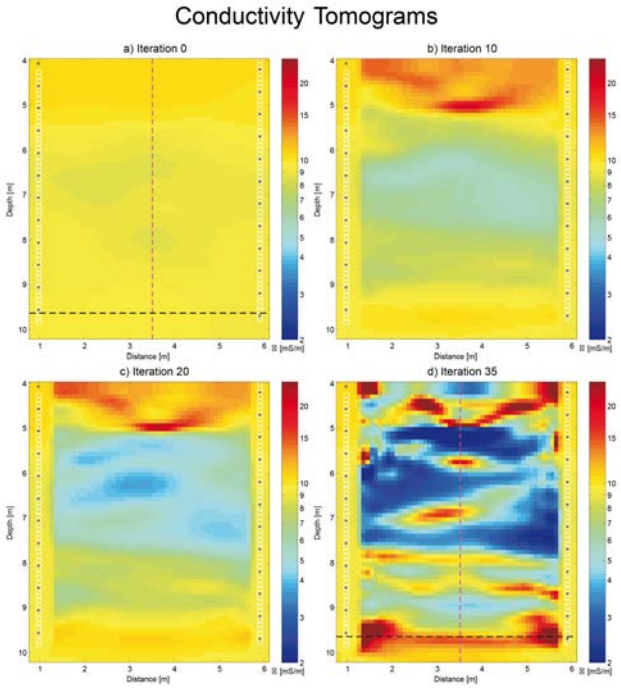

Figure C12. Conductivity tomograms for different iteration steps from (a) initial model of the full-waveform inversion obtained from the ray-based inversion, (b), (c) and (d) show the models obtained at iterations 10, 20 and 35, respectively. The dashed black line refers to Figure C15b, where a comparison Natural Gamma logging data is presented. This line indicates the resolved underlying lacustrine sediments. The violet dashed line indicates the position of the logging boreholes (2.5 m away).

A.3.6 RMS convergence

The RMS misfit between observed and predicted traces is shown in Figure C13. The vertical axis is normalized such that the RMS of the initial model (obtained with the ray based inversion) is equal to 1.0. The convergence criterion of less than 1% change in the misfit between iterations is achieved after 35 iterations.

A.3.7 Comparison between observed and modeled traces

Figure C14 compares the observed traces (red) for transmitter positions 2, 7 and 11 at iteration 35 with the modeled traces (blue). A very good fit between the synthetic and measured traces is apparent. The agreement for transmitter 2 (Figure C14a) is less convincing, which is probably due to transmitter 2 being located in the upper region close to the water table (see arrow in Figure C14a), where the additional refractions and reflections (not included in the modeled data) are strongly present. Note that transmitter 2 was excluded from the source wavelet estimation. Due to the presence of the water table, the obtained model is probably unreliable for the depth range between 4m and 6 m. Instead of discarding the traces containing refracted waves which have travelled through the unsaturated gravel, as is done in the ray-based inversion (see Figure C5c), we included all traces in the full-waveform inversion. The algorithm tried to fit these events without taking into account the presence of the unsaturated zone. The presence of the water-table is indicated by the prominent reflections shown in the blue ellipse in Figure C14 for transmitter 2 in the upper 5 traces. This probably produces anomalous structures (low and high permittivity and conductivity values) in the upper 2 m. To improve these results, data above the water table should be measured and included in the inversion. The full-waveform inversion should be able to fit these critically refracted waves and reflected waves when a proper starting model is used, which includes this zone

For transmitters 7 and 11 (Figure C14b and c), the simulated amplitudes and phases fit the measured data remarkably well. Therefore, we expect that the tomogram details below 6 m depth represent reality rather well. By comparing Figures C8, C10 and C14 it is obvious that the fit between the observed and synthetic data becomes significantly better after wavelet estimation and especially after the full-waveform inversion. The green ellipses indicate the areas with the best fit. All these results indicate that the simultaneous full-waveform inversion of both permittivity and conductivity performs well!

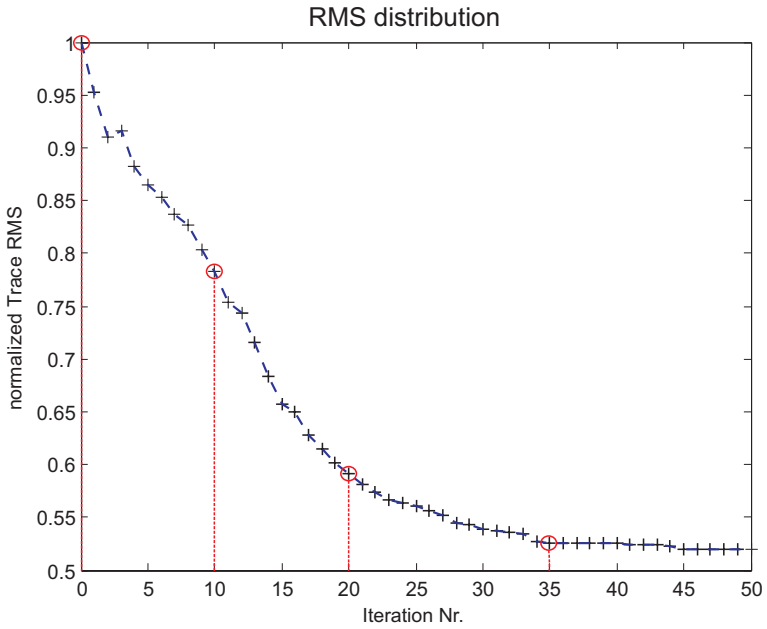

Figure C13. RMS values as a function of iteration number for the ray-based inversion starting model. The RMS is normalized to the ray-based inversion result and after 35 iterations the RMS misfit changes less than 1%. The red circles along the graph indicate the iteration number for which the permittivity and conductivity results are shown in Figures C11 and C12.

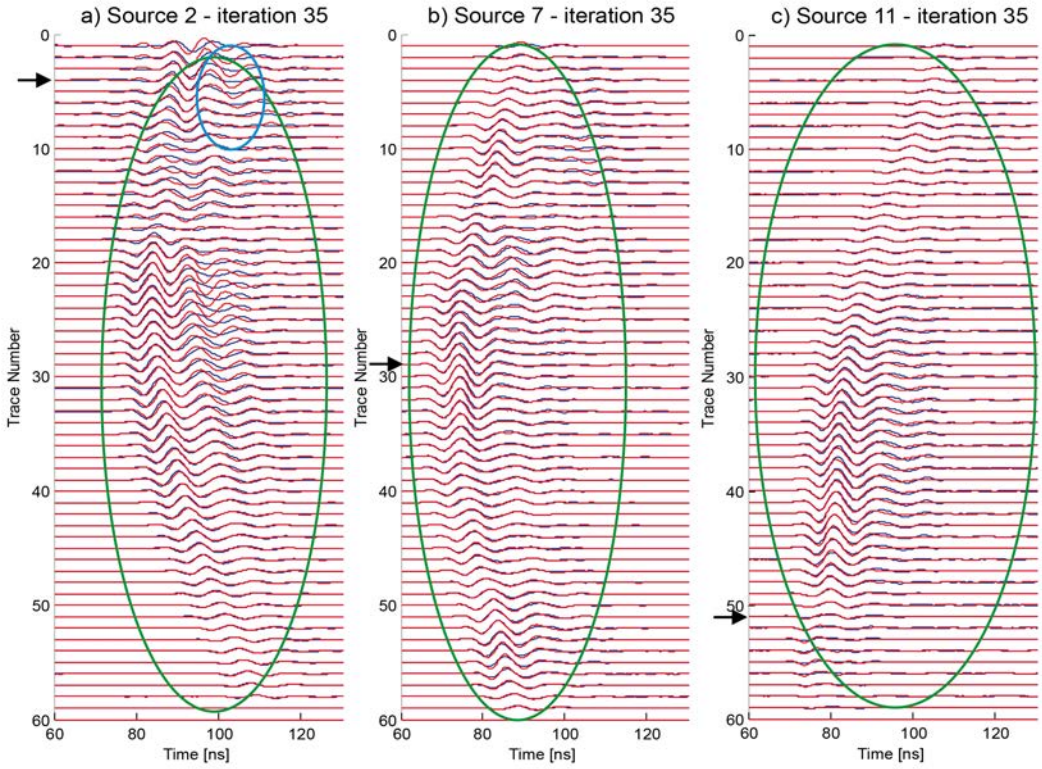

Figure C14. Un-normalized traces after 35 iterations for the measurements of transmitters (a) 2, (b) 7 and (c) 11. A general good agreement of the observed traces (red) and the simulated traces (blue) is visible. The green ellipses indicating where the fit is best between the traces, whereas the blue ellipse shows the reflections from the water table (see text for further discussion).

A.3.8 Interpretation and comparison with borehole logging data

The permittivity is influenced mainly by the pore structure and the porosity of the gravel, which contains particle sizes between 0.2 mm and 60 mm [*Füchtenbauer*, 1988; *Diem et al.*, 2010] and also a small fraction of fines. Permittivity values for saturated gravel are reported to lie between 20 to 30 [*Daniels et al.*, 2005]. The conductivity is determined by porosity and pore structure, salinity, and surface conductivity at the grain/solution interface. Moreover, if clay is present in the gravel, conductivities will increase with an increasing amount of clay. Clay particles contribute the exchange of cations to the electrolyte, which increases the conductivity of the formation [*Waxman and Smits*, 1968; *Worthington*, 1993].

To assess the reliability of the full-waveform results we analyzed geophysical borehole logs acquired at two wells located at either side, 2.5 m distance away from the crosshole plane. The plane between these north-east (P11) and south-west (P13) boreholes cross our tomographic plane at the center (indicated by the violet dashed line in Figure C11d and C12d). Neutron-Neutron data indicate water content (and thus porosity), whereas Natural Gamma data indicate the presence of clay. Neutron-Neutron logs are transformed into porosity using the approach and parameters of *Barrash and Clemo* [2002] for both boreholes P11 and P13 and plotted in Figure C15a in blue and cyan, respectively. The obtained permittivities for the traveltime (I=0) and full-waveform inversion (I=35) at the center of the planes (see dashed violet lines in Figure C11a and d) are converted to porosity using the petrophysical model of Linde *et al.* [2006a] with the parameters of Chapter 2 and plotted in Figure C15a in red and green, respectively.

Without any additional calibration, the values obtained for the converted Neutron-Neutron logs and permittivity results are very close and similar vertical variations can be observed. Especially from 6.8 m to 7.3 m and from 8.5 m to 9.3 m the porosity values for P13 fit very well the inversion results and from 7.8 m to 8.3 m the values for P11 fit well the inversion results. Note that both borehole logs indicate a lateral variation and the curves shown in Figure C15 represent porosity values 2.5 m away from each other. In future, the borehole logs should be taken at the center of the tomographic plane to enable a direct comparison.

In Figure C15b, the obtained conductivities for the traveltime (I=0) and full-waveform inversion (I=35) at the center of the planes (see dashed violet lines in Figure C12a and d) are plotted in Figure C15b in red and green, respectively. The dashed black line in Figure C15b indicate the high conductivity zone in the tomographic plane at the base of the aquifer below

9.6 m depth (see also black dashed line in Figure C12d), which indicates the boundary of the lacustrine sediment. These results fit very well with the Natural Gamma logs of P11 and P13 (blue and cyan lines in Figure C15b) that clearly indicate the presence of a high clay content layer below 9.6 m. The Neutron-Neutron results also indicate a strong discontinuity at the same depth level. Note that these lacustrine sediments could not be resolved with the ray-based inversion. As expected, a poor match is found between the borehole logs and the tomograms within the uppermost 2 m.

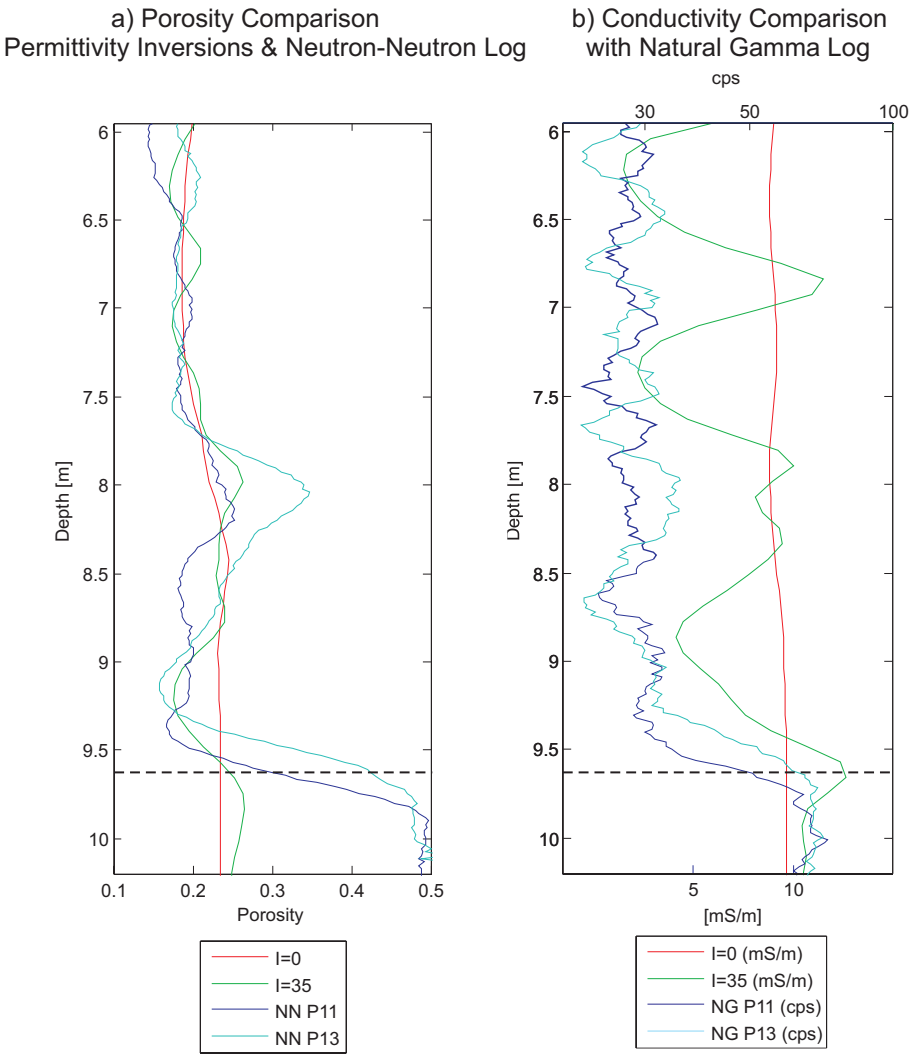

Figure C15. (a) Comparison of the Neutron porosities of the boreholes P11 and P13 with the porosities obtained from the permittivities observed at the same level for the ray-based inversion result (I=0) and the final solution of the full-waveform inversion (I=35) over the depth interval 6 m to 10.2 m. (b) Comparison of the Natural Gamma counts for both boreholes with the conductivity observed at the same level for the ray-based inversion (I=0) and the final solution of the full-waveform inversion (I=35) over the depth interval 6 m to 10.2 m. All graphs are plotted logarithmically. Note that the lacustrine sediments (clays) are indicated by the black dashed line (compare with the dashed line in Figure C12d).

A.4 CONCLUSIONS AND OUTLOOK

A recently developed full-waveform inversion algorithm for crosshole GPR data [*Meles et al.*, 2010] was optimized by introducing an improved acquisition setup. Using a limited number of transmitter positions and many more receiver positions, the acquisition time and the computational cost (memory and CPU time) could be reduced compared to a conventional setup that uses an equal number of transmitter and receiver positions. To improve the low ray-coverage close to the transmitter borehole, a semi-reciprocal setup was employed which entailed populating the original receiver borehole with new transmitter positions (and conversely populating the original transmitter borehole with a dense array of receiver positions). This approach has been evaluated by analyzing crosshole GPR data acquired within an aquifer composed of gravelly river deposits and resulted in a good data fit between the measured traces and the synthetic traces. As expected, the permittivity and conductivity tomograms obtained are much more detailed than conventional ray-based inversion results.

The obtained results are compared with Neutron-Neutron and Natural Gamma logging data measured at either side, 2.5 m distance away from the crosshole plane. The inverted permittivity values and the measured Neutron-Neutron logs are converted to porosities using conversions described in literature and show very similar absolute values and vertical variations with high resolution. At some depth ranges a good correspondence is observed for one of the logs whereas at other depths this is observed for the other log. This is explained by the presence of lateral variation observed in the two Neutron-Neutron borehole logs measured at either side, 2.5 m distance away from the crosshole plane, such that a direct comparison is not possible. Note that the ray-based permittivity tomogram only provided low resolution porosity information. The full-waveform conductivity tomogram indicates an increased conductivity below 9.6 m at all lateral positions, which corresponds to the lacustrine sediments. Comparison of the conductivity tomogram with the Natural Gamma logs confirms that the thick clay layer at the base of the aquifer is present at a depth of approximately 9.6 m. The Neutron-Neutron logs also indicated a strong discontinuity below this depth. Note that this layer was not clearly identified in the ray-based conductivity tomogram.

Comparison with ERT models obtained in Chapter 4 indicates that the electrical conductivities at a center frequency of 100 MHz obtained by full-waveform inversion are approximately 50% higher than those obtained by the ERT inversion (DC or low frequency values). This apparent discrepancy may be explained by the frequency-dependency of

electrical conductivity [*Knight and Nur*, 1987]. This needs to be investigated further in future work.

Thin horizontal layers were imaged for the upper part (4 m to 5.5m) of the aquifer having strongly alternating permittivities and conductivities, but no agreement with the borehole logs was found. On the basis of the poor match of the observed and predicted traces in the upper part of the aquifer (Figure C14a), we expect the full-waveform models to be unreliable in this region. A likely explanation for this is the presence of the groundwater table, which represents a very strong discontinuity in electrical subsurface parameters. This leads to non-linear effects that can cause the inversion to get trapped in local minima. A possible solution would be to incorporate the water table as à priori information in the initial model, to increase the model space and to use transmitters in the unsaturated zone. Another factor that might also influence the results in the upper part of the aquifer is the 3-D to 2-D conversion, which is only valid for far-field conditions. Here, the minimum distance between transmitter and receiver is seven wavelengths and recent publications [*Streich and van der Kruk*, 2007a] indicate that the far-field assumption may be thus not valid. The use of a 2½ D forward modeling program [e.g., *Bing and Greenhalgh*, 1998a] might solve this problem.

Our analyses showed that estimation of the source wavelet is critical. A possible improvement could be the estimation of an effective source wavelet for different areas, where the medium parameters and the corresponding dielectric coupling are different [*Tronicke and Holliger*, 2004]. Instead of assuming a point source, it would also be possible to implement finite antennas in the modeling [*Streich and van der Kruk*, 2007b], to consider the real dimensions of the antennas. Until now, only a source wavelet correction is applied before the full-waveform inversion, but the source wavelet could be updated after a few iterations and possibly the results can be further improved.

In summary, we optimized the acquisition setup and incorporated this in the full-waveform inversion of crosshole GPR measurements such that the acquisition time and computational costs are significantly reduced. The permittivity and conductivity images of the gravel aquifer show a much higher resolution compared to the ray-based inversion (see Figures C11 and C12). For the first time, high conductivity lacustrine sediments underlying a gravel aquifer were imaged using full-waveform inversion of crosshole GPR data, in correspondence with Natural Gamma logs. In addition, high resolution porosity values were obtained having similar vertical changes as the Neutron-Neutron logs. Since the logs and the inversion plane were not co-located, direct comparison was not possible, but the obtained

results show that this approach has high potential to characterize and image gravel aquifers for hydrological purposes.

REFERENCES

Acworth, R. I., and Dasey, G. R., 2003. Mapping of the hyporheic zone around a tidal creek using a combination of borehole logging, borehole electrical tomography and cross-creek electrical imaging, New South Wales, Australia, *Hydrogeology Journal*, **11**, 368-377.

Ajo-Franklin, J. B., Minsley, B. J., and Daley, T. M., 2007. Applying compactness constraints to differential traveltime tomography, *Geophysics*, **72**, R67-R75.

al Hagrey, S. A., and Müller, C., 2000. GPR study of pore water content and salinity in sand, *Geophysical Prospecting*, **48**, 63-85.

Allègre, V., Jouniaux, L., Lehmann, F., and Sailhac, P., 2010. Streaming potential dependence on water-content in Fontainebleau sand, *Geophysical Journal International*, **182**, 1248-1266.

Alumbaugh, D., Chang, P. Y., Paprocki, L., Brainard, J. R., Glass, R. J., and Rautman, C. A., 2002. Estimating moisture contents in the vadose zone using cross-borehole ground penetrating radar: A study of accuracy and repeatability, *Water Resources Research*, **38**, 1309.

Alumbaugh, D. L., and Newman, G. A., 2000. Image appraisal for 2-D and 3-D electromagnetic inversion, *Geophysics*, **65**, 1455-1467.

Annan, A. P., 2005. GPR Methods for Hydrogeological Studies, in *Hydrogeophysics*, edited by Y. Rubin and S. S. Hubbard, pp. 185-213, Springer Netherlands.

Archie, G. E., 1942. The electrical resistivity log as an aid in determining some reservoir characteristics, *Transactions of the American institute of Mining, Metallurgical and Petroleum Engineers*, **146**, 54-62.

Arora, T., Linde, N., Revil, A., and Castermant, J., 2007. Non-intrusive characterization of the redox potential of landfill leachate plumes from self-potential data, *Journal of Contaminant Hydrology*, **92**, 274-292.

Aubert, M., and Yéené Atangana, Q., 1996. Self-potential method in hydrogeological exploration of volcanic areas, *Ground Water*, **34**, 1010-1016.

Avseth, P., Mukerji, T., Jørstad, A., Mavko, G., and Veggeland, T., 2001. Seismic reservoir mapping from 3-D AVO in a North Sea turbidite system, *Geophysics*, **66**, 1157-1176.

BAFU, 2010. Hydrologischer Atlas der Schweiz, *Bundeamt für Umwelt, Bern, Switzerland*.

Barrash, W., and Clemo, T., 2002. Hierarchical geostatistics and multifacies systems: Boise Hydrogeophysical Research Site, Boise, Idaho, *Water Resources Research*, **38**, 1196.

Barrenetxea, G., Ingelrest, F., Schaefer, G., and Vetterli, M., 2008. The hitchhiker's guide to successful wireless sensor network deployments, *Sensys'08: Proceedings of the 6th Acm Conference on Embedded Networked Sensor Systems*, 43-56.

Battin, T. J., and Sengschmitt, D., 1999. Linking sediment biofilms, hydrodynamics, and river bed clogging: Evidence from a large river, *Microbial Ecology*, **37**, 185-196.

Baumann, M., Jordan, P., Hoehn, E., and Geisser, H., 2009. Ein neues Grundwassermodell für das Thurtal, *Mitteilungen der Thurgauischen Naturforschenden Gesellschaft*, **63**.

Bedrosian, P. A., Maercklin, N., Weckmann, U., Bartov, Y., Ryberg, T., and Ritter, O., 2007. Lithology-derived structure classification from the joint interpretation of magnetotelluric and seismic models, *Geophysical Journal International*, **170**, 737-748.

Bélanger, C., Giroux, B., Gloaguen, E., and Lefebvre, R., 2010. GPR, ERT and CPT data integration for high resolution aquifer modeling, *13th International Conference on GPR*, 1-6.

Belghoul, A., 2007. *Caractérisation petrophysique et hydrodynamique du socle cristallin*: PhD thesis, University of Montpellier.

Belina, F. A., Ernst, J. R., and Holliger, K., 2009. Inversion of crosshole seismic data in heterogeneous environments: Comparison of waveform and ray-based approaches, *Journal of Applied Geophysics*, **68**, 85-94.

Bencala, K. E., 1984. Interactions of solutes and streambed sediment 2. A dynamic analysis of coupled hydrologic and chemical processes that determine solute transport, *Water Resources Research*, **20**, 1804-1814.

Beres, M., Green, A., Huggenberger, P., and Horstmeyer, H., 1995. Mapping the architecture of glaciofluvial sediments with 3-dimensional georadar, *Geology*, **23**, 1087-1090.

Beres, M., Huggenberger, P., Green, A. G., and Horstmeyer, H., 1999. Using two- and three-dimensional georadar methods to characterize glaciofluvial architecture, *Sedimentary Geology*, **129**, 1-24.

Bernhardt, E. S., Palmer, M. A., Allan, J. D., Alexander, G., Barnas, K., et al., 2005. Ecology - Synthesizing US river restoration efforts, *Science*, **308**, 636-637.

Beutel, J., Dyer, M., Lim, R., Plessl, C., Wohrle, M., et al., 2007. Automated wireless sensor network testing, *INSS 07: Proceedings of the Fourth International Conference on Networked Sensing Systems*, 303-303.

Beven, K., and Binley, A., 1992. The future of distributed models - model calibration and uncertainty prediction, *Hydrological Processes*, **6**, 279-298.

Bing, Z., and Greenhalgh, S. A., 1998a. A damping method for the computation of the 2.5-D Green's function for arbitrary acoustic media, *Geophysical Journal International*, **133**, 111-120.

Bing, Z., and Greenhalgh, S. A., 1998b. Crosshole acoustic velocity imaging with full-waveform spectral data: 2.5-D numerical simulations, *Exploration Geophysics*, **29**, 680-684.

Bing, Z., and Greenhalgh, S. A., 2000. Cross-hole resistivity tomography using different electrode configurations, *Geophysical Prospecting*, **48**, 887-912.

Binley, A., Winship, P., Middleton, R., Pokar, M., and West, J., 2001. High-resolution characterization of vadose zone dynamics using cross-borehole radar, *Water Resources Research*, **37**, 2639-2652.

Binley, A., Winship, P., West, L. J., Pokar, M., and Middleton, R., 2002a. Seasonal variation of moisture content in unsaturated sandstone inferred from borehole radar and resistivity profiles, *Journal of Hydrology*, **267**, 160-172.

Binley, A., Cassiani, G., Middleton, R., and Winship, P., 2002b. Vadose zone flow model parameterisation using cross-borehole radar and resistivity imaging, *Journal of Hydrology*, **267**, 147-159.

Binley, A., Cassiani, G., and Deiana, R., 2010. Hydrogeophysics: Opportunities and challenges, *Bollettino di Geofisica Teorica ed Applicata*, **51**, 267-284.

Birchak, J. R., Gardner, C. G., Hipp, J. E., and Victor, J. M., 1974. High dielectric constant microwave probes for sensing soil moisture, *Proceedings of the IEEE*, **62**, 93-98.

Bleistein, N., 1986. 2-1/2 dimensional inplane wave-propagation, *Geophysical Prospecting*, **34**, 686-703.

Blome, M., Maurer, H. R., and Schmidt, K., 2009. Advances in three-dimensional geoelectric forward solver techniques, *Geophysical Journal International*, **176**, 740-752.

Blome, M., Maurer, H., and Greenhalgh, S., 2011. Geoelectric experimental design - Efficient acquisition and exploitation of complete pole-bipole data sets, *Geophysics*, **76**, F15-F26.

Boggs, J. M., and Adams, E. E., 1992. Field study of dispersion in a heterogeneous aquifer: 4. Investigation of adsorption and sampling bias, *Water Resources Research*, **28**, 3325-3336.

Boggs, J. M., Young, S. C., Beard, L. M., Gelhar, L. W., Rehfeldt, K. R., and Adams, E. E., 1992. Field-study of dispersion in a heterogeneous aquifer: 1. Overview and site description, *Water Resources Research*, **28**, 3281-3291.

Bohlen, T., 2002. Parallel 3-D viscoelastic finite difference seismic modelling, *Computers & Geosciences*, **28**, 887-899.

Bolève, A., Revil, A., Janod, F., Mattiuzzo, J. L., and Fry, J. J., 2009. Preferential fluid flow pathways in embankment dams imaged by self-potential tomography, *Near Surface Geophysics*, **7**, 447-462.

Bosma, T. N. P., Ballemans, E. M. W., Hoekstra, N. K., teWelscher, R. A. G., Smeenk, J. G. M. M., et al., 1996. Biotransformation of organics in soil columns and an infiltration area, *Ground Water*, **34**, 49-56.

Bouman, C. A., 1997. Cluster: An unsupervised algorithm for modeling Gaussian mixtures, http://www.ece.purdue.edu/~bouman.

Bourg, A. C. M., and Bertin, C., 1993. Biogeochemical processes during the infiltration of river water into an alluvial aquifer, *Environmental Science & Technology*, **27**, 661-666.

Bouwer, H., and Rice, R. C., 1976. Slug test for determining hydraulic conductivity of unconfined aquifers with completely or partially penetrating wells, *Water Resources Research*, **12**, 423-428.

Bowling, J. C., Rodriguez, A. B., Harry, D. L., and Zheng, C., 2005. Delineating alluvial aquifer heterogeneity using resistivity and GPR data, *Ground Water*, **43**, 890-903.

Bowling, J. C., Harry, D. L., Rodriguez, A. B., and Zheng, C., 2007. Integrated geophysical and geological investigation of a heterogeneous fluvial aquifer in Columbus Mississippi, *Journal of Applied Geophysics*, **62**, 58-73.

Bradford, J. H., Clement, W. P., and Barrash, W., 2009. Estimating porosity with ground-penetrating radar reflection tomography: A controlled 3-D experiment at the Boise Hydrogeophysical Research Site, *Water Resources Research*, **45**, W00D26.

Brookes, A., 1988. *Channelized rivers: Prospectives for environmental management*, John Wiley and Sons, Chichester, UK.

Brovelli, A., and Cassiani, G., 2010. A combination of the Hashin-Shtrikman bounds aimed at modelling electrical conductivity and permittivity of variably saturated porous media, *Geophysical Journal International*, **180**, 225-237.

Brunke, M., and Gonser, T., 1997. The ecological significance of exchange processes between rivers and groundwater, *Freshwater Biology*, **37**, 1-33.

Butler, A. P., Mathias, S. A., Gallagher, A. J., Peach, D. W., and Williams, A. T., 2009. Analysis of flow processes in fractured chalk under pumped and ambient conditions (UK), *Hydrogeology Journal*, **17**, 1849-1858.

Butler, J. J., 1998. *The design, performance and analysis of slug tests*, Lewis, Boca Raton.

Butler, J. J., Garnett, E. J., and Healey, J. M., 2003. Analysis of slug tests in formations of high hydraulic conductivity, *Ground Water*, **41**, 620-630.

BUWAL, 2004. Wegleitung Grundwasserschutz, *Bundesamt für Umwelt, Wald und Landschaft, Bern, Switzerland*.

Carcione, J. M., Ursin, B., and Nordskag, J. I., 2007. Cross-property relations between electrical conductivity and the seismic velocity of rocks, *Geophysics*, **72**, E193-E204.

Cardenas, M. B., Wilson, J. L., and Zlotnik, V. A., 2004. Impact of heterogeneity, bed forms, and stream curvature on subchannel hyporheic exchange, *Water Resources Research*, **40**, W08307.

Cardenas, M. B., and Markowski, M. S., 2011. Geoelectrical imaging of hyporheic exchange and mixing of river water and groundwater in a large regulated river, *Environmental Science & Technology*, **45**, 1407-1411.

Carsel, R. F., and Parrish, R. S., 1988. Developing joint probability-distributions of soil-water retention characteristics, *Water Resources Research*, **24**, 755-769.

Caruthers, R. M., and Smith, I. F., 1992. The use of ground electrical survey methods for siting water-supply boreholes in shallow crystalline basement terrains, in *Hydrogeology of Crystalline Basement Aquifers in Africa*, edited by E. P. Wright and W. G. Burgess, pp. 203-220, Geological Society Special Publication.

Cassiani, G., Bruno, V., Villa, A., Fusi, N., and Binley, A. M., 2006. A saline trace test monitored via time-lapse surface electrical resistivity tomography, *Journal of Applied Geophysics*, **59**, 244-259.

Chambers, J. E., Wilkinson, P. B., Weller, A. L., Meldrum, P. I., Gilvy, R. D., and Caunt, S., 2007. Mineshaft imaging using surface and crosshole 3D electrical resistivity tomography: A case history from the East Pennine Coalfield, UK, *Journal of Applied Geophysics*, **62**, 324-337.

Chen, J. S., Hubbard, S., Rubin, Y., Murray, C., Roden, E., and Majer, E., 2004. Geochemical characterization using geophysical data and Markov Chain Monte Carlo methods: A case

study at the South Oyster bacterial transport site in Virginia, *Water Resources Research*, **40**, W12412.

Cirpka, O. A., Fienen, M. N., Hofer, M., Hoehn, E., Tessarini, A., et al., 2007. Analyzing bank filtration by deconvoluting time series of electric conductivity, *Ground Water*, **45**, 318-328.

Claerbout, J. F., and Muir, F., 1973. Robust modeling with erratic data, *Geophysics*, **38**, 826-844.

Constantz, J., Cox, M. H., and Su, G. W., 2003. Comparison of heat and bromide as ground water tracers near streams, *Ground Water*, **41**, 647-656.

Constantz, J., 2008. Heat as a tracer to determine streambed water exchanges, *Water Resources Research*, **44**, W00D10.

Coscia, I., Marescot, L., Maurer, H., Greenhalgh, S., and Linde, N., 2008. Experimental design for crosshole electrical resistivity tomography data sets, *14th Annual European Meeting of Environmental and Engineering Geophysics, EAGE.*

Coscia, I., Greenhalgh, S., Linde, N., Green, A., Günther, T., et al., 2010. A multi-borehole 3-D ERT monitoring system for aquifer characterization using river flood events as a natural tracer, *16th Annual European Meeting of Environmental and Engineering Geophysics, EAGE.*

Coscia, I., Greenhalgh, S. A., Linde, N., Doetsch, J., Marescot, L., et al., 2011a. 3D crosshole ERT for aquifer characterization and monitoring of infiltrating river water, *Geophysics*, **76**, G49-G59.

Coscia, I., Linde, N., Greenhalgh, S., Günther, T., and Green, A., 2011b. A deconvolution approach to correct time-lapse 3D ERT data and improve imaging of natural aquifer dynamics, *Water Resources Research*, under review.

Crook, N., Binley, A., Knight, R., Robinson, D. A., Zarnetske, J., and Haggerty, R., 2008. Electrical resistivity imaging of the architecture of substream sediments, *Water Resources Research*, **44**, W00D13.

Daily, W., and Owen, E., 1991. Cross-borehole resistivity tomography, *Geophysics*, **56**, 1228-1235.

Daily, W., Ramirez, A., Labrecque, D., and Nitao, J., 1992. Electrical resistivity tomography of vadose water movement, *Water Resources Research*, **28**, 1429-1442.

Daily, W., and Ramirez, A., 1995. Electrical-resistance tomography during in-situ trichloroethylene remediation at the savanna river site, *Journal of Applied Geophysics*, **33**, 239-249.

Daily, W., Ramirez, A., Binley, A., and LaBrecque, D., 2005. Electrical resistance tomography — theory and practice, in *Near surface geophysics*, edited by D. K. Butler, pp. 525-550, SEG.

Daniels, J. J., Allred, B., Binley, A., Labrecque, D., and Alumbaugh, D., 2005. Hydrogeophysical case studies in the vadose zone, in *Hydrogeophysics*, edited by Y. Rubin and S. S. Hubbard, pp. 413-440, Springer.

Darling, T., 2005. *Well logging and formation evaluation*, Elsevier.

Darnet, M., and Marquis, G., 2004. Modelling streaming potential (SP) signals induced by water movement in the vadose zone, *Journal of Hydrology*, **285**, 114-124.

Day-Lewis, F. D., Lane, J. W., Jr., Harris, J. M., and Gorelick, S. M., 2003. Time-lapse imaging of saline-tracer transport in fractured rock using difference-attenuation radar tomography, *Water Resources Research*, **39**, 1290.

Day-Lewis, F. D., and Lane, J. W., 2004. Assessing the resolution-dependent utility of tomograms for geostatistics, *Geophysical Research Letters*, **31**, L07503.

Day-Lewis, F. D., Singha, K., and Binley, A. M., 2005. Applying petrophysical models to radar travel time and electrical resistivity tomograms: Resolution-dependent limitations, *Journal of Geophysical Research-Solid Earth*, **110**, B08206.

Day-Lewis, F. D., Lane, J. W., and Gorelick, S. M., 2006. Combined interpretation of radar, hydraulic, and tracer data from a fractured-rock aquifer near Mirror Lake, New Hampshire, USA, *Hydrogeology Journal*, **14**, 1-14.

Day-Lewis, F. D., Chen, Y., and Singha, K., 2007. Moment inference from tomograms, *Geophysical Research Letters*, **34**, L22404.

de Franco, R., Biella, G., Tosi, L., Teatini, P., Lozej, A., et al., 2009. Monitoring the saltwater intrusion by time lapse electrical resistivity tomography: The Chioggia test site (Venice Lagoon, Italy), *Journal of Applied Geophysics*, **69**, 117-130.

Deiana, R., Cassiani, G., Kemna, A., Villa, A., Bruno, V., and Bagliani, A., 2007. An experiment of non-invasive characterization of the vadose zone via water injection and cross-hole time-lapse geophysical monitoring, *Near Surface Geophysics*, **5**, 183-194.

Dempster, A. P., Laird, N. M., and Rubin, D. B., 1977. Maximum likelihood from incomplete data via the EM algorithm, *Journal of the Royal Statistical Society, Series B (Methodological)*, **39**, 1-38.

Deutsch, C. V., and Journel, A. G., 1998. *GSLIB: Geostatistical software library and user's guide*, 2. edition ed., Oxford Univ. Press, New York, 2. edition.

Diem, S., Vogt, T., and Hoehn, E., 2010. Räumliche Charakterisierung der hydraulischen Leitfähigkeit in alluvialen Schotter-Grundwasserleitern: Ein Methodenvergleich, *Grundwasser*, **15**, 241-251.

Dietrich, C. R., and Newsam, G. N., 1997. Fast and exact simulation of stationary Gaussian processes through circulant embedding of the covariance matrix, *Siam Journal on Scientific Computing*, **18**, 1088-1107.

Dogan, M., Van Dam, R. L., Bohling, G. C., Butler, J. J., Jr., and Hyndman, D. W., 2011. Hydrostratigraphic analysis of the MADE site with full-resolution GPR and direct-push hydraulic profiling, *Geophysical Research Letters*, **38**, L06405.

Dorn, C., Linde, N., Le Borgne, T., Bour, O., and Baron, L., 2011. Single-hole GPR reflection imaging of solute transport in a granitic aquifer, *Geophysical Research Letters*, **38**, L08401.

Doussan, C., Jouniaux, L., and Thony, J. L., 2002. Variations of self-potential and unsaturated water flow with time in sandy loam and clay loam soils, *Journal of Hydrology*, **267**, 173-185.

EC, 2000. Directive 2000/60/EC of the European Parliament and of the council establishing a framework for community action in the field of water policy, *Official Journal of the European Community*, **L327**, 1-72.

Eckert, P., Lamberts, R., and Wagner, C., 2008. The impact of climate change on drinking water supply by riverbank filtration, *Water Science Technology*, **8**, 319-324.

Edmaier, K., Burlando, P., and Perona, P., 2011. Mechanisms of vegetation uprooting by flow in alluvial non-cohesive sediment, *Hydrology and Earth Systems Science Discussion*, **8**, 1365-1398.

Eisenberg, D., and Kauzmann, W., 1969. *The structure and properties of water*, Oxford University Press.

Ellis, R. G., and Oldenburg, D. W., 1994. Applied geophysical inversion, *Geophysical Journal International*, **116**, 5-11.

Eppstein, M. J., and Dougherty, D. E., 1998. Optimal 3-D traveltime tomography, *Geophysics*, **63**, 1053-1061.

Ernst, J. R., Maurer, H., Green, A. G., and Holliger, K., 2007a. Full-waveform inversion of crosshole radar data based on 2-D finite-difference time-domain solutions of Maxwell's equations, *Ieee Transactions on Geoscience and Remote Sensing*, **45**, 2807-2828.

Ernst, J. R., Green, A. G., Maurer, H., and Holliger, K., 2007b. Application of a new 2D time-domain full-waveform inversion scheme to crosshole radar data, *Geophysics*, **72**, J53-J64.

Ernst, J. R., 2007. *2-D finite-difference time-domain full-waveform inversion of crosshole georadar data*: PhD thesis, ETH Zurich.

Farquharson, C. G., 2008. Constructing piecewise-constant models in multidimensional minimum-structure inversions, *Geophysics*, **73**, K1-K9.

Favetto, A., Pomposiello, C., Booker, J., and Rossello, E. A., 2007. Magnetotelluric inversion constrained by seismic data in the Tucuman basin (Andean foothills, 27 degrees S, NW argentina), *Journal of Geophysical Research - Solid Earth*, **112**, B09104.

Fine, R. A., and Millero, F. J., 1973. Compressibility of water as a function of temperature and pressure, *Journal of Chemical Physics*, **59**, 5529-5536.

Fleckenstein, J. H., Niswonger, R. G., and Fogg, G. E., 2006. River-aquifer interactions, geologic heterogeneity, and low-flow management, *Ground Water*, **44**, 837-852.

Fournier, C., 1989. Spontaneous potentials and resistivity surveys applied to hydrogeology in a volcanic area - case-history of the Chaine-Des-Puys (Puy-De-Dome, France), *Geophysical Prospecting*, **37**, 647-668.

Fregoso, E., and Gallardo, L. A., 2009. Cross-gradients joint 3D inversion with applications to gravity and magnetic data, *Geophysics*, **74**, L31-L42.

French, H., and Binley, A., 2004. Snowmelt infiltration: Monitoring temporal and spatial variability using time-lapse electrical resistivity, *Journal of Hydrology*, **297**, 174-186.

Friedel, S., 2003. Resolution, stability and efficiency of resistivity tomography estimated from a generalized inverse approach, *Geophysical Journal International*, **153**, 305-316.

Friedel, S., Byrdina, S., Jacobs, F., and Zimmer, M., 2004. Self-potential and ground temperature at Merapi volcano prior to its crisis in the rainy season of 2000-2001, *Journal of Volcanology and Geothermal Research*, **134**, 149-168.

Füchtenbauer, H., 1988. *Sedimente und Sedimentgesteine: Sandsteine*, 4 ed., Schweizerbart, Stuttgart.

Gallardo, L. A., and Meju, M. A., 2003. Characterization of heterogeneous near-surface materials by joint 2D inversion of dc resistivity and seismic data, *Geophysical Research Letters*, **30**, 1658.

Gallardo, L. A., and Meju, M. A., 2004. Joint two-dimensional DC resistivity and seismic travel time inversion with cross-gradients constraints, *Journal of Geophysical Research - Solid Earth*, **109**, B03311.

Gallardo, L. A., Meju, M. A., and Pérez-Flores, M. A., 2005. A quadratic programming approach for joint image reconstruction: Mathematical and geophysical examples, *Inverse Problems*, **21**, 435-452.

Gallardo, L. A., 2007. Multiple cross-gradient joint inversion for geospectral imaging, *Geophysical Research Letters*, **34**, L19301.

Gallardo, L. A., and Meju, M. A., 2007. Joint two-dimensional cross-gradient imaging of magnetotelluric and seismic traveltime data for structural and lithological classification, *Geophysical Journal International*, **169**, 1261-1272.

Gallardo, L. A., and Meju, M. A., 2011. Structure-Coupled Multiphysics Imaging in Geophysical Sciences, *Reviews of Geophysics*, **49**, RG1003.

Garambois, S., Senechal, P., and Perroud, H., 2002. On the use of combined geophysical methods to assess water content and water conductivity of near-surface formations, *Journal of Hydrology*, **259**, 32-48.

Gasperikova, E., Zhang, Y., and Hubbard, S., 2008. Using self potential and multiphase flow modeling to optimize groundwater pumping*, EOS Transactions AGU, 89(53).*

Giannopoulos, A., 2005. Modelling ground penetrating radar by GprMax, *Construction and Building Materials*, **19**, 755-762.

Gibert, D., and Pessel, M., 2001. Identification of sources of potential fields with the continuous wavelet transform: Application to self-potential profiles, *Geophysical Research Letters*, **28**, 1863-1866.

Golub, G. H., and van Loan, C. F., 1996. *Matrix computations*, Johns Hopkins University Press.

Gooseff, M. N., Anderson, J. K., Wondzell, S. M., LaNier, J., and Haggerty, R., 2005. A modelling study of hyporheic exchange pattern and the sequence, size, and spacing of stream bedforms in mountain stream networks, Oregon, USA, *Hydrological Processes*, **19**, 2915-2929.

Grasmueck, M., 1996. 3-D ground-penetrating radar applied to fracture imaging in gneiss, *Geophysics*, **61**, 1050-1064.

Grinsted, A., Moore, J. C., and Jevrejeva, S., 2004. Application of the cross wavelet transform and wavelet coherence to geophysical time series, *Nonlinear Processes in Geophysics*, **11**, 561-566.

GschG, 1991. Gewaesserschutzgesetz,, *Bundesgesetz über den Schutz der Gewässer, Schweiz*, **814.20**, 30.

GSchV, 1998. Gewaesserschutzverordnung, *Bundesgesetz über den Schutz der Gewässer, Schweiz*, **814.201**, 60.

Günther, T., 2004. *Inversion methods and resolution analysis for the 2D/3D reconstruction of resistivity structures from DC measurements*, Ph.D. thesis thesis: TU Bergakademie Freiberg.

Günther, T., and Rücker, C., 2006. A general approach for introducing information into inversion and examples from dc resistivity inversion, in *14th Annual European Meeting of Environmental and Engineering Geophysics*, edited, p. P039, EAGE.

Günther, T., Rücker, C., and Spitzer, K., 2006. Three-dimensional modelling and inversion of dc resistivity data incorporating topography - II. Inversion, *Geophysical Journal International*, **166**, 506-517.

Günther, T., and Rücker, C., 2009. Advanced inversion strategies using a new geophysical inversion and modelling library, *15th Annual European Meeting of Environmental and Engineering Geophysics, EAGE.*

Haber, E., and Oldenburg, D., 1997. Joint inversion: A structural approach, *Inverse Problems*, **13**, 63-77.

Harbaugh, A. W., 2005. MODFLOW-2005, The U.S. Geological Survey modular ground-water model—the ground-water flow process, in *Book 6. Modeling techniques*, Ch. 16.

Harvey, J. W., and Bencala, K. E., 1993. The effect of streambed topography on surface-subsurface water exchange in mountain catchments, *Water Resources Research*, **29**, 89-98.

Hashin, Z., and Shtrikman, S., 1962. A variational approach to theory of effective magnetic permeability of multiphase materials, *Journal of Applied Physics*, **33**, 3125-&.

Hashin, Z., and Shtrikman, S., 1963. A variational approach to the theory of the elastic behaviour of multiphase materials, *Journal of the Mechanics and Physics of Solids*, **11**, 127-140.

Hatch, C. E., Fisher, A. T., Revenaugh, J. S., Constantz, J., and Ruehl, C., 2006. Quantifying surface water-groundwater interactions using time series analysis of streambed thermal records: Method development, *Water Resources Research*, **42**, W10410.

Hauck, C., 2002. Frozen ground monitoring using DC resistivity tomography, *Geophysical Research Letters*, **29**, 2016.

Hayley, K., Bentley, L. R., and Gharibi, M., 2009. Time-lapse electrical resistivity monitoring of salt-affected soil and groundwater, *Water Resources Research*, **45**.

Heinz, J., Kleineidam, S., Teutsch, G., and Aigner, T., 2003. Heterogeneity patterns of quaternary glaciofluvial gravel bodies (SW-Germany): Application to hydrogeology, *Sedimentary Geology*, **158**, 1-23.

Henderson, R. D., Day-Lewis, F. D., and Harvey, C. F., 2009. Investigation of aquifer-estuary interaction using wavelet analysis of fiber-optic temperature data, *Geophysical Research Letters*, **36**, L06403.

Hiscock, K. M., and Grischek, T., 2002. Attenuation of groundwater pollution by bank filtration, *Journal of Hydrology*, **266**, 139-144.

Hoehn, E., and Cirpka, O. A., 2006. Assessing residence times of hyporheic ground water in two alluvial flood plains of the Southern Alps using water temperature and tracers, *Hydrology and Earth System Sciences*, **10**, 553-563.

Hoehn, E., and Scholtis, A., 2011. Exchange between a river and groundwater, assessed with hydrochemical data, *Hydrology and Earth System Sciences*, **15**, 983-988.

Hollender, F., Tillard, S., and Corin, L., 1999. Multifold borehole radar acquisition and processing, *Geophysical Prospecting*, **47**, 1077-1090.

Holliger, K., Musil, M., and Maurer, H. R., 2001. Ray-based amplitude tomography for crosshole georadar data: A numerical assessment, *Journal of Applied Geophysics*, **47**, 285-298.

Hu, W. Y., Abubakar, A., and Habashy, T. M., 2009. Joint electromagnetic and seismic inversion using structural constraints, *Geophysics*, **74**, R99-R109.

Hubbard, S., and Linde, N., 2011. Hydrogeophysics, in *Treatise on water*, edited by P. Wilderer, Ch. 43, Elsevier.

Hubbard, S. S., Rubin, Y., and Majer, E., 1999. Spatial correlation structure estimation using geophysical and hydrogeological data, *Water Resources Research*, **35**, 1809-1825.

Hubbard, S. S., Chen, J. S., Peterson, J., Majer, E. L., Williams, K. H., et al., 2001. Hydrogeological characterization of the South Oyster Bacterial Transport Site using geophysical data, *Water Resources Research*, **37**, 2431-2456.

Huggenberger, P., 1993. Radar facies: Recognition of facies patterns and heterogeneities within Pleistocene Rhine gravels, NE Switzerland, *Geological Society, London, Special Publications*, **75**, 163-176.

Huggenberger, P., Hoehn, E., Beschta, R., and Woessner, W., 1998. Abiotic aspects of channels and floodplains in riparian ecology, *Freshwater Biology*, **40**, 407-425.

Hyndman, D. W., and Gorelick, S. M., 1996. Estimating lithologic and transport properties in three dimensions using seismic and tracer data: The Kesterson aquifer, *Water Resources Research*, **32**, 2659-2670.

Hyndman, D. W., and Harris, J. M., 1996. Traveltime inversion for the geometry of aquifer lithologies, *Geophysics*, **61**, 1728-1737.

Jackson, M. D., 2010. Multiphase electrokinetic coupling: Insights into the impact of fluid and charge distribution at the pore scale from a bundle of capillary tubes model, *Journal of Geophysical Research-Solid Earth*, **115**, B07206.

Jacobs, L. A., Vongunten, H. R., Keil, R., and Kuslys, M., 1988. Geochemical changes along a river-groundwater infiltration flow path - Glattfelden, Switzerland, *Geochimica Et Cosmochimica Acta*, **52**, 2693-2706.

Jakubowicz, H., 1990. A simple efficient method of dip-moveout correction, *Geophysical Prospecting*, **38**, 221-245.

Jardani, A., Revil, A., Boleve, A., Crespy, A., Dupont, J. P., et al., 2007. Tomography of the Darcy velocity from self-potential measurements, *Geophysical Research Letters*, **34**, L24403.

Jayawickreme, D. H., Van Dam, R. L., and Hyndman, D. W., 2008. Subsurface imaging of vegetation, climate, and root-zone moisture interactions, *Geophysical Research Letters*, **35**, L18404.

Jegen, M. D., Hobbs, R. W., Tarits, P., and Chave, A., 2009. Joint inversion of marine magnetotelluric and gravity data incorporating seismic constraints: Preliminary results of sub-basalt imaging off the Faroe Shelf, *Earth and Planetary Science Letters*, **282**, 47-55.

Jougnot, D., Ghorbani, A., Revil, A., Leroy, P., and Cosenza, P., 2010. Spectral induced polarization of partially saturated clay-rocks: A mechanistic approach, *Geophysical Journal International*, **180**, 210-224.

Jung, H. K., Min, D. J., Lee, H. S., Oh, S., and Chung, H., 2009. Negative apparent resistivity in dipole-dipole electrical surveys, *Exploration Geophysics*, **40**, 33-40.

Kalbus, E., Reinstorf, F., and Schirmer, M., 2006. Measuring methods for groundwater - surface water interactions: A review, *Hydrology and Earth System Sciences*, **10**, 873-887.

Kalbus, E., Schmidt, C., Molson, J. W., Reinstorf, F., and Schirmer, M., 2009. Influence of aquifer and streambed heterogeneity on the distribution of groundwater discharge, *Hydrology and Earth System Sciences*, **13**, 69-77.

Keery, J., Binley, A., Crook, N., and Smith, J. W. N., 2007. Temporal and spatial variability of groundwater-surface water fluxes: Development and application of an analytical method using temperature time series, *Journal of Hydrology*, **336**, 1-16.

Keller, G. V., and Frischknecht, F., 1966. *Electrical methods in geophysical prospecting*, Pergamon.

Kemna, A., Kulessa, B., and Vereecken, H., 2002. Imaging and characterisation of subsurface solute transport using electrical resistivity tomography (ERT) and equivalent transport models, *Journal of Hydrology*, **267**, 125-146.

Khalil, A. A., Stewart, R. R., and Henley, D. C., 1993. Full-wave-form processing and interpretation of kilohertz cross-well seismic data, *Geophysics*, **58**, 1248-1256.

Kipfer, R., Aeschbach-Hertig, W., Peeters, F., and Stute, M., 2002. Noble gases in lakes and ground waters, *Noble Gases in Geochemistry and Cosmochemistry*, **47**, 615-700.

Klotzsche, A., van der Kruk, J., Meles, G. A., Doetsch, J., Maurer, H., and Linde, N., 2010. Full-waveform inversion of cross-hole ground-penetrating radar data to characterize a gravel aquifer close to the Thur River, Switzerland, *Near Surface Geophysics*, **8**, 635-649.

Knight, R. J., and Nur, A., 1987. The dielectric-constant of sandstones, 60 Khz to 4 Mhz, *Geophysics*, **52**, 644-654.

Koch, K., Wenninger, J., Uhlenbrook, S., and Bonell, M., 2009. Joint interpretation of hydrological and geophysical data: Electrical resistivity tomography results from a process hydrological research site in the Black Forest Mountains, Germany, *Hydrological Processes*, **23**, 1501-1513.

Kondolf, G. M., 1998. Lessons learned from river restoration projects in California, *Aquatic Conservation-Marine and Freshwater Ecosystems*, **8**, 39-52.

Kosinski, W. K., and Kelly, W. E., 1981. Geoelectric soundings for predicting aquifer properties, *Ground Water*, **19**, 163-171.

Kowalsky, M. B., Finsterle, S., Peterson, J., Hubbard, S., Rubin, Y., et al., 2005. Estimation of field-scale soil hydraulic and dielectric parameters through joint inversion of GPR and hydrological data, *Water Resources Research*, **41**, W11425.

Krautblatter, M., Verleysdonk, S., Flores-Orozco, A., and Kemna, A., 2010. Temperature-calibrated imaging of seasonal changes in permafrost rock walls by quantitative electrical resistivity

tomography (Zugspitze, German/Austrian Alps), *Journal of Geophysical Research-Earth Surface*, **115**, F02003.

Kruse, S., Grasmueck, M., Weiss, M., and Viggiano, D., 2006. Sinkhole structure imaging in covered Karst terrain, *Geophysical Research Letters*, **33**, L16405.

Kumar, P., and Foufoula-Georgiou, E., 1997. Wavelet analysis for geophysical applications, *Reviews of Geophysics*, **35**, 385-412.

Kuras, O., Pritchard, J. D., Meldrum, P. I., Chambers, J. E., Wilkinson, P. B., et al., 2009. Monitoring hydraulic processes with automated time-lapse electrical resistivity tomography (ALERT), *Comptes Rendus Geoscience*, **341**, 868-885.

Kuroda, S., Takeuchi, M., and Kim, H. J., 2007. Full-waveform inversion algorithm for interpreting crosshole radar data: A theoretical approach, *Geosciences Journal*, **11**, 211-217.

LaBrecque, D. J., Ramirez, A. L., Daily, W. D., Binley, A. M., and Schima, S. A., 1996a. ERT monitoring on environmental remediation processes, *Measurement Science & Technology*, **7**, 375-383.

LaBrecque, D. J., Miletto, M., Daily, W., Ramirez, A., and Owen, E., 1996b. The effects of noise on Occam's inversion of resistivity tomography data, *Geophysics*, **61**, 538-548.

LaBrecque, D. J., and Yang, X., 2001. Difference inversion of ERT data: A fast inversion method for 3-D in situ monitoring, *Journal of Environmental and Engineering Geophysics*, **6**, 83-89.

Lacey, G., 1930. Stable channel in alluvium, *Proceedings of the Institution of Civil Engineers*, **229**, 259-292.

Lane, J. W., Day-Lewis, F. D., and Casey, C. C., 2006. Geophysical monitoring of a field-scale biostimulation pilot project, *Ground Water*, **44**, 430-443.

Langevin, C. D., Thorne, D. T., Jr., Dausman, A. M., Sukip, M. C., and Guo, W., 2008. SEAWAT version 4: A computer program for simulation of multi-species solute and heat transport, in *USGS Techniques and Methods Book 6*, Ch. A22.

Langevin, C. D., 2009. SEAWAT: A computer program for simulation of variable-density groundwater flow and multi-species solute and heat transport, *U.S. Geological Survey*, Fact Sheet 2009-3047.

Lanz, E., Boerner, D. E., Maurer, H., and Green, A., 1998. Landfill delineation and characterization using electrical, electromagnetic and magnetic methods, *Journal of Environmental and Engineering Geophysics*, **3**, 185-196.

Lazaratos, S. K., Harris, J. M., Rector, J. W., and Vanschaack, M., 1995. High-resolution crosswell imaging of a west texas carbonate reservoir 4. Reflection imaging, *Geophysics*, **60**, 702-711.

Le Borgne, T., Bour, O., Paillet, F. L., and Caudal, J. P., 2006. Assessment of preferential flow path connectivity, and hydraulic properties at single-borehole and cross-borehole scales in a fractured aquifer, *Journal of Hydrology*, **328**, 347-359.

Le Borgne, T., Bour, O., Riley, M. S., Gouze, P., Pezard, P. A., et al., 2007. Comparison of alternative methodologies for identifying and characterizing preferential flow paths in heterogeneous aquifers, *Journal of Hydrology*, **345**, 134-148.

Leonard, B. P., 1991. The ULTIMATE conservative difference scheme applied to unsteady one-dimensional advection, *Computer Methods in Applied Mechanics and Engineering*, **88**, 17-74.

Lesmes, D. P., and Friedman, S. P., 2005. Relationships between the electrical and hydrogeological properties of rocks and soils, in *Hydrogeophysics*, edited by Y. Rubin and S. S. Hubbard, pp. 87-128, Springer.

Li, S. H., Unsworth, M. J., Booker, J. R., Wei, W. B., Tan, H. D., and Jones, A. G., 2003. Partial melt or aqueous fluid in the mid-crust of Southern Tibet? Constraints from INDEPTH magnetotelluric data, *Geophysical Journal International*, **153**, 289-304.

Linde, N., Binley, A., Tryggvason, A., Pedersen, L. B., and Revil, A., 2006a. Improved hydrogeophysical characterization using joint inversion of cross-hole electrical resistance and ground-penetrating radar traveltime data, *Water Resources Research*, **42**, W12404.

Linde, N., Finsterle, S., and Hubbard, S., 2006b. Inversion of tracer test data using tomographic constraints, *Water Resources Research*, **42**, W04410.

Linde, N., Jougnot, D., Revil, A., Matthäi, S. K., Arora, T., et al., 2007a. Streaming current generation in two-phase flow conditions, *Geophysical Research Letters*, **34**, L03306.

Linde, N., and Revil, A., 2007. Inverting self-potential data for redox potentials of contaminant plumes, *Geophysical Research Letters*, **34**, L14302.

Linde, N., Revil, A., Bolève, A., Dagès, C., Castermant, J., et al., 2007b. Estimation of the water table throughout a catchment using self-potential and piezometric data in a Bayesian framework, *Journal of Hydrology*, **334**, 88-98.

Linde, N., Tryggvason, A., Peterson, J. E., and Hubbard, S. S., 2008. Joint inversion of crosshole radar and seismic traveltimes acquired at the South Oyster Bacterial Transport Site, *Geophysics*, **73**, G29-G37.

Linde, N., and Doetsch, J. A., 2010. Joint inversion of crosshole GPR and seismic traveltime data, in *Advances in near-surface seismology and ground-penetrating radar*, edited by R. D. Miller, J. H. Bradford and K. Holliger, Ch. 1, pp. 1-18, Society of Exploration Geophysicists.

Linde, N., Doetsch, J., Jougnot, D., Genoni, O., Dürst, Y., et al., 2011. Self-potential investigations of a gravel bar in a restored river corridor, *Hydrology and Earth System Sciences*, **15**, 729-742.

Lines, L. R., Schultz, A. K., and Treitel, S., 1988. Cooperative inversion of geophysical data, *Geophysics*, **53**, 8-20.

Loke, M. H., and Barker, R. D., 1996. Practical techniques for 3D resistivity surveys and data inversion, *Geophysical Prospecting*, **44**, 499-523.

Long, J. C. S., Aydin, A., Brown, S. R., Einstein, H. H., Hestir, K., et al., 1996. *Rock fracture and fluid flow: Contemporary understanding and applications*, National Academy Press, Washington, DC.

Looms, M. C., Jensen, K. H., Binley, A., and Nielsen, L., 2008. Monitoring unsaturated flow and transport using cross-borehole geophysical methods, *Vadose Zone Journal*, **7**, 227.

Lowry, T., Allen, M. B., and Shive, P. N., 1989. Singularity removal: A refinement of resistivity modeling techniques, *Geophysics*, **54**, 766-774.

Lunt, I. A., Bridge, J. S., and Tye, R. S., 2004. A quantitative three-dimensional depositional model of gravelly braided rivers, *Sedimentology*, **51**, 1155-1155.

Maineult, A., Bernabe, Y., and Ackerer, P., 2004. Electrical response of flow, diffusion, and advection in a laboratory sand box, *Vadose Zone Journal*, **3**, 1180-1192.

Maineult, A., Bernabe, Y., and Ackerer, P., 2005. Detection of advected concentration and pH fronts from self-potential measurements, *Journal of Geophysical Research-Solid Earth*, **110**, B11205.

Maineult, A., Strobach, E., and Renner, J., 2008. Self-potential signals induced by periodic pumping tests, *Journal of Geophysical Research-Solid Earth*, **113**, B01203.

Mair, J. A., and Green, A. G., 1981. High-resolution seismic-reflection profiles reveal fracture-zones within a homogeneous granite batholith, *Nature*, **294**, 439-442.

Maraun, D., and Kurths, J., 2004. Cross wavelet analysis: Significance testing and pitfalls, *Nonlinear Processes in Geophysics*, **11**, 505-514.

Marescot, L., Rigobert, S., P. Lopes, S., Lagabrielle, R., and Chapellier, D., 2006. A general approach for DC apparent resistivity evaluation on arbitrarily shaped 3D structures, *Journal of Applied Geophysics*, **60**, 55-67.

Maurer, H., Holliger, K., and Boerner, D. E., 1998. Stochastic regularization: Smoothness or similarity?, *Geophysical Research Letters*, **25**, 2889-2892.

Maurer, H., and Musil, M., 2004. Effects and removal of systematic errors in crosshole georadar attenuation tomography, *Journal of Applied Geophysics*, **55**, 261-270.

Maurer, H., and Friedel, S., 2006. Outer-space sensitivities in geoelectrical tomography, *Geophysics*, **71**, G93-G96.

Maurer, H., Friedel, S., and Jaeggi, D., 2009. Characterization of a coastal aquifer using seismic and geoelectric borehole methods, *Near Surface Geophysics*, **7**, 353-366.

Mazac, O., Kelly, W. E., and Landa, I., 1987. Surface geoelectrics for groundwater pollution and protection studies, *Journal of Hydrology*, **93**, 277-294.

McClymont, A. F., Green, A. G., Streich, R., Horstmeyer, H., Tronicke, J., et al., 2008. Visualization of active faults using geometric attributes of 3D GPR data: An example from the Alpine Fault Zone, New Zealand, *Geophysics*, **73**, B11-B23.

McElwee, C. D., and Zenner, M. A., 1998. A nonlinear model for analysis of slug-test data, *Water Resources Research*, **34**, 55-66.

Meles, G. A., Van der Kruk, J., Greenhalgh, S. A., Ernst, J. R., Maurer, H., and Green, A. G., 2010. A new vector waveform inversion algorithm for simultaneous updating of conductivity and permittivity parameters from combination crosshole/borehole-to-surface GPR data, *Ieee Transactions on Geoscience and Remote Sensing*, **48**, 3391-3407.

Merkli, B., 1975. *Untersuchungen über Mechanismen und Kinetik der Elimination von Bakterien und Viren im Grundwasser*: ETH Zurich.

Miall, A. D., 1995. Description and interpretation of fluvial deposits - A critical perspective, *Sedimentology*, **42**, 379-384.

Michel, S., Salehi, A., Luo, L., Dawes, N., Aberer, K., et al., 2009. Environmental monitoring 2.0, *Icde: 2009 Ieee 25th International Conference on Data Engineering, Vols. 1-3*, 1507-1510.

Michot, D., Benderitter, Y., Dorigny, A., Nicoullaud, B., King, D., and Tabbagh, A., 2003. Spatial and temporal monitoring of soil water content with an irrigated corn crop cover using surface electrical resistivity tomography, *Water Resources Research*, **39**, 1138.

Miller, C. R., Routh, P. S., Brosten, T. R., and McNamara, J. P., 2008. Application of time-lapse ERT imaging to watershed characterization, *Geophysics*, **73**, G7-G17.

Minsley, B. J., 2007. *Modeling and inversion of self-potential data*: PhD thesis, Massachusetts Institute of Technology.

Minsley, B. J., Sogade, J., and Morgan, F. D., 2007. Three-dimensional source inversion of self-potential data, *Journal of Geophysical Research*, **112**.

Mitchell, T. M., 1997. *Machine learning*, McGraw-Hill, New York.

Monego, M., Cassiani, G., Deiana, R., Putti, M., Passadore, G., and Altissimo, L., 2010. A tracer test in a shallow heterogeneous aquifer monitored via time-lapse surface electrical resistivity tomography, *Geophysics*, **75**, WA61-WA73.

Monteiro Santos, F. A., Sultan, S. A., Represas, P., and El Sorady, A. L., 2006. Joint inversion of gravity and geoelectrical data for groundwater and structural investigation: Application to the northwestern part of Sinai, Egypt, *Geophysical Journal International*, **165**, 705-718.

Mora, P., 1987. Nonlinear two-dimensional elastic inversion of multioffset seismic data, *Geophysics*, **52**, 1211-1228.

Müller, K., Vanderborght, J., Englert, A., Kemna, A., Huisman, J. A., et al., 2010. Imaging and characterization of solute transport during two tracer tests in a shallow aquifer using electrical resistivity tomography and multilevel groundwater samplers, *Water Resources Research*, **46**, W03502.

Musil, M., Maurer, H. R., and Green, A. G., 2003. Discrete tomography and joint inversion for loosely connected or unconnected physical properties: Application to crosshole seismic and georadar data sets, *Geophysical Journal International*, **153**, 389-402.

Nadeau, D. F., Brutsaert, W., Parlange, M. B., Bou-Zeid, E., Barrenetxea, G., et al., 2009. Estimation of urban sensible heat flux using a dense wireless network of observations, *Environmental Fluid Mechanics*, **9**, 635-653.

Nimmer, R. E., Osiensky, J. L., Binley, A. M., Sprenke, K. F., and Williams, B. C., 2007. Electrical resistivity imaging of conductive plume dilution in fractured rock, *Hydrogeology Journal*, **15**, 877-890.

Nimmer, R. E., Osiensky, J. L., Binley, A. M., and Williams, B. C., 2008. Three-dimensional effects causing artifacts in two-dimensional, cross-borehole, electrical imaging, *Journal of Hydrology*, **359**, 59-70.

Nyquist, J. E., Freyer, P. A., and Toran, L., 2008. Stream bottom resistivity tomography to map ground water discharge, *Ground Water*, **46**, 561-569.

Ogilvy, R. D., Meldrum, P. I., Kuras, O., Wilkinson, P. B., Chambers, J. E., et al., 2009. Automated monitoring of coastal aquifers with electrical resistivity tomography, *Near Surface Geophysics*, **7**, 367-375.

Oldenburg, D. W., and Li, Y. G., 1999. Estimating depth of investigation in dc resistivity and IP surveys, *Geophysics*, **64**, 403-416.

Olsson, O., Falk, L., Forslund, O., Lundmark, L., and Sandberg, E., 1992. Borehole radar applied to the characterization of hydraulically conductive fracture-zones in crystalline rock, *Geophysical Prospecting*, **40**, 109-142.

Oreskes, N., Shrader-Frechette, K., and Belitz, K., 1994. Verification, validation, and confirmation of numerical models in the earth sciences, *Science*, **263**, 641-646.

Orghidan, T., 1959. Ein neuer Lebensraum des unterirdischen Wassers: der hyporheische Biotop, *Arch. Hydrobiol.*, **55**, 392-414.

Osiensky, J. L., Nimmer, R., and Binley, A. M., 2004. Borehole cylindrical noise during hole-surface and hole-hole resistivity measurements, *Journal of Hydrology*, **289**, 78-94.

Paasche, H., Tronicke, J., Holliger, K., Green, A. G., and Maurer, H., 2006. Integration of diverse physical-property models: Subsurface zonation and petrophysical parameter estimation based on fuzzy c-means cluster analyses, *Geophysics*, **71**, H33-H44.

Paasche, H., and Tronicke, J., 2007. Cooperative inversion of 2D geophysical data sets: A zonal approach based on fuzzy c-means cluster analysis, *Geophysics*, **72**, A35-A39.

Paasche, H., Wendrich, A., Tronicke, J., and Trela, C., 2008. Detecting voids in masonry by cooperatively inverting P-wave and georadar traveltimes, *Journal of Geophysics and Engineering*, **5**, 256-267.

Paige, C. C., and Saunders, M. A., 1982. LSQR: An algorithm for sparse linear equations and sparse least squares, *ACM Transactions on Mathematical Software*, **8**, 43-71.

Palmer, M. A., Bernhardt, E. S., Allan, J. D., Lake, P. S., Alexander, G., et al., 2005. Standards for ecologically successful river restoration, *Journal of Applied Ecology*, **42**, 208-217.

Park, S. K., Johnston, M. J. S., Madden, T. R., Morgan, F. D., and Morrison, H. F., 1993. Electromagnetic precursors to earthquakes in the ULF band - a review of observations and mechanisms, *Reviews of Geophysics*, **31**, 117-132.

Parker, R. L., 1984. The inverse problem of resistivity sounding, *Geophysics*, **49**, 2143-2158.

Pasquale, N., Perona, P., Schneider, P., Shrestha, J., Wombacher, A., and Burlando, P., 2011. Modern comprehensive approach to monitor the morphodynamic evolution of a restored river corridor, *Hydrology and Earth System Sciences*, **15**, 1197-1212.

Perrier, F., and Morat, P., 2000. Characterization of electrical daily variations induced by capillary flow in the non-saturated zone, *Pure and Applied Geophysics*, **157**, 785-810.

Petiau, G., 2000. Second generation of lead-lead chloride electrodes for geophysical applications, *Pure and Applied Geophysics*, **157**, 357-382.

Podvin, P., and Lecomte, I., 1991. Finite difference computation of traveltimes in very contrasted velocity models: A massively parallel approach and its associated tools, *Geophysical Journal International*, **105**, 271-284.

Pollock, D., and Cirpka, O. A., 2010. Fully coupled hydrogeophysical inversion of synthetic salt tracer experiments, *Water Resources Research*, **46**, W07501.

Portniaguine, O., and Zhdanov, M. S., 1999. Focusing geophysical inversion images, *Geophysics*, **64**, 874-887.

Pratt, R. G., 1999. Seismic waveform inversion in the frequency domain, part 1: Theory and verification in a physical scale model, *Geophysics*, **64**, 888-901.

Pratt, R. G., and Shipp, R. M., 1999. Seismic waveform inversion in the frequency domain, part 2: Fault delineation in sediments using crosshole data, *Geophysics*, **64**, 902-914.

Pride, S., 1994. Governing equations for the coupled electromagnetics and acoustics of porous-media, *Physical Review B*, **50**, 15678-15696.

Pride, S. R., Berryman, J. G., and Harris, J. M., 2004. Seismic attenuation due to wave-induced flow, *Journal of Geophysical Research-Solid Earth*, **109**, B01201.

Pruess, K., Oldenburg, C. M., and Moridis, G. J., 1999. TOUGH2 user's guide version 2, Rep. LBNL--43134, 204 pp, Lawrence Berkeley National Laboratory.

Ptak, T., and Teutsch, G., 1994. Forced and natural gradient tracer tests in a highly heterogeneous porous aquifer - instrumentation and measurements, *Journal of Hydrology*, **159**, 79-104.

Ramirez, A., Daily, W., Labrecque, D., Owen, E., and Chesnut, D., 1993. Monitoring an underground steam injection process using electrical-resistance tomography, *Water Resources Research*, **29**, 73-87.

Ranguelova, E. B., 2002. *Segmentation of textured images on three-dimensional lattices*: PhD thesis, University of Dublin.

RECORD, 2011. Assessment and modeling of coupled ecological and hydrological dynamics in the restored corridor of the river, *Competence Center Environment and Sustainability*, http://www.cces.ethz.ch/projects/nature/Record.

Regli, C., Rauber, M., and Huggenberger, P., 2003. Analysis of aquifer heterogeneity within a well capture zone, comparison of model data with field experiments: A case study from the river Wiese, Switzerland, *Aquatic Sciences*, **65**, 111-128.

Revil, A., Cathles, L. M., Losh, S., and Nunn, J. A., 1998. Electrical conductivity in shaly sands with geophysical applications, *Journal of Geophysical Research - Solid Earth*, **103**, 23925-23936.

Revil, A., and Cathles, L. M., 1999. Permeability of shaly sands, *Water Resources Research*, **35**, 651-662.

Revil, A., Naudet, V., Nouzaret, J., and Pessel, M., 2003. Principles of electrography applied to self-potential electrokinetic sources and hydrogeological applications, *Water Resources Research*, **39**, 1114.

Revil, A., and Leroy, P., 2004. Constitutive equations for ionic transport in porous shales, *Journal of Geophysical Research-Solid Earth*, **109**, B03208.

Revil, A., and Linde, N., 2006. Chemico-electromechanical coupling in microporous media, *Journal of Colloid and Interface Science*, **302**, 682-694.

Revil, A., Linde, N., Cerepi, A., Jougnot, D., Matthai, S., and Finsterle, S., 2007. Electrokinetic coupling in unsaturated porous media, *Journal of Colloid and Interface Science*, **313**, 315-327.

Revil, A., Trolard, F., Bourrie, G., Castermant, J., Jardani, A., and Mendonca, C. A., 2009. Ionic contribution to the self-potential signals associated with a redox front, *Journal of Contaminant Hydrology*, **109**, 27-39.

Rizzo, E., Suski, B., Revil, A., Straface, S., and Troisi, S., 2004. Self-potential signals associated with pumping tests experiments, *Journal of Geophysical Research-Solid Earth*, **109**, B10203.

Robinson, D. A., Binley, A., Crook, N., Day-Lewis, F. D., Ferre, T. P. A., et al., 2008. Advancing process-based watershed hydrological research using near-surface geophysics: A vision for, and review of, electrical and magnetic geophysical methods, *Hydrological Processes*, **22**, 3604-3635.

Rubin, Y., and Hubbard, S. S. (Eds.), 2005. *Hydrogeophysics*, Springer, Dordrecht, The Netherlands.

Rücker, C., Günther, T., and Spitzer, K., 2006. Three-dimensional modelling and inversion of dc resistivity data incorporating topography - I. Modelling, *Geophysical Journal International*, **166**, 495-505.

Ruelleu, S., Moreau, F., Bour, O., Gapais, D., and Martelet, G., 2010. Impact of gently dipping discontinuities on basement aquifer recharge: An example from Ploemeur (Brittany, France), *Journal of Applied Geophysics*, **70**, 161-168.

Samaritani, E., Shrestha, J., Fournier, B., Frossard, E., Gillet, F., et al., 2011. Heterogeneity of soil carbon pools and fluxes in a channelized and a restored floodplain section (Thur River, Switzerland), *Hydrology and Earth System Sciences Discussions*, **8**, 1059-1091.

Sambridge, M., Braun, J., and Mcqueen, H., 1995. Geophysical parametrization and interpolation of irregular data using natural neighbors, *Geophysical Journal International*, **122**, 837-857.

Sandberg, S. K., Slater, L. D., and Versteeg, R., 2002. An integrated geophysical investigation of the hydrogeology of an anisotropic unconfined aquifer, *Journal of Hydrology*, **267**, 227-243.

Saracco, G., Labazuy, P., and Moreau, F., 2004. Localization of self-potential sources in volcano-electric effect with complex continuous wavelet transform and electrical tomography methods for an active volcano, *Geophysical Research Letters*, **31**, L12610.

Schälchli, U., 1992. The clogging of coarse gravel river beds by fine sediment, *Hydrobiologia*, **235-236**, 189-197.

Schälchli, U., 2008. Geschiebehaushalt im Thurgebiet, *Wasser Energie Luft*, **100**, 23-28.

Schäppi, B., Perona, P., Schneider, P., and Burlando, P., 2010. Integrating river cross section measurements with digital terrain models for improved flow modelling applications, *Computers & Geosciences*, **36**, 707-716.

Scheibe, T. D., and Chien, Y. J., 2003. An evaluation of conditioning data for solute transport prediction, *Ground Water*, **41**, 128-141.

Schmidt, C., Bayer-Raich, M., and Schirmer, M., 2006. Characterization of spatial heterogeneity of groundwater-stream water interactions using multiple depth streambed temperature measurements at the reach scale, *Hydrology and Earth System Sciences*, **10**, 849-859.

Schmidt, C., Conant, B., Bayer-Raich, M., and Schirmer, M., 2007. Evaluation and field-scale application of an analytical method to quantify groundwater discharge using mapped streambed temperatures, *Journal of Hydrology*, **347**, 292-307.

Schneider, P., Vogt, T., Schirmer, M., Doetsch, J., Linde, N., et al., 2011. Towards improved instrumentation for assessing river-groundwater interactions in a restored river corridor, *Hydrology and Earth System Sciences*, **15**, 2531-2549.

Schön, J. H., 1996. *Physical properties of rocks: Fundamentals and principles of petrophysics*, Elsevier Science Publishing Company, Inc.

Schulmeister, M. K., Butler, J. J., Healey, J. M., Zheng, L., Wysocki, D. A., and McCall, G. W., 2003. Direct-push electrical conductivity logging for high-resolution hydrostratigraphic characterization, *Ground Water Monitoring and Remediation*, **23**, 52-62.

Schwarzenbach, R. P., and Westall, J., 1981. Transport of non-polar organic-compounds from surface-water to groundwater - Laboratory sorption studies, *Environmental Science & Technology*, **15**, 1360-1367.

Schwarzenbach, R. P., Giger, W., Hoehn, E., and Schneider, J. K., 1983. Behavior of organic-compounds during infiltration of river water to groundwater - Field studies, *Environmental Science & Technology*, **17**, 472-479.

Schwarzenbach, R. P., Escher, B. I., Fenner, K., Hofstetter, T. B., Johnson, C. A., et al., 2006. The challenge of micropollutants in aquatic systems, *Science*, **313**, 1072-1077.

Seiz, G., and Foppa, N., 2007. Nationales Klima-Beobachtungssystem (GCOS Schweiz), *Bundesamt für Meteorologie und Klimatologie, MeteoSchweiz und ProClim, Bern, Switzerland*.

Selker, J. S., Thevenaz, L., Huwald, H., Mallet, A., Luxemburg, W., et al., 2006. Distributed fiber-optic temperature sensing for hydrologic systems, *Water Resources Research*, **42**, W12202.

Sen, P. N., Scala, C., and Cohen, M. H., 1981. A self-similar model for sedimentary-rocks with application to the dielectric-constant of fused glass-beads, *Geophysics*, **46**, 781-795.

Shankar, V., Eckert, P., Ojha, C. S. P., and Konig, C. M., 2009. Transient three-dimensional modeling of riverbank filtration at Grind well field, Germany, *Hydrogeology Journal*, **17**, 321-326.

Sheffer, M. R., and Oldenburg, D. W., 2007. Three-dimensional modelling of streaming potential, *Geophysical Journal International*, **169**, 839-848.

Sill, W. R., 1983. Self-potential modeling from primary flows, *Geophysics*, **48**, 76-86.

Silliman, S. E., and Booth, D. F., 1993. Analysis of time-series measurements of sediment temperature for identification of gaining vs losing portions of Juday-Creek, Indiana, *Journal of Hydrology*, **146**, 131-148.

Singha, K., and Gorelick, S. M., 2005. Saline tracer visualized with three-dimensional electrical resistivity tomography: Field-scale spatial moment analysis, *Water Resources Research*, **41**, W05023.

Sjödahl, P., Dahlin, T., and Johansson, S., 2009. Embankment dam seepage evaluation from resistivity monitoring data, *Near Surface Geophysics*, **7**, 463-474.

Slater, L., and Sandberg, S. K., 2000. Resistivity and induced polarization monitoring of salt transport under natural hydraulic gradients, *Geophysics*, **65**, 408-420.

Slater, L., Binley, A. M., Daily, W., and Johnson, R., 2000. Cross-hole electrical imaging of a controlled saline tracer injection, *Journal of Applied Geophysics*, **44**, 85-102.

Slater, L., and Binley, A., 2006. Synthetic and field-based electrical imaging of a zerovalent iron barrier: Implications for monitoring long-term barrier performance, *Geophysics*, **71**, B129-B137.

Slob, E., Sato, M., and Olhoeft, G., 2010. Surface and borehole ground-penetrating-radar developments, *Geophysics*, **75**, A103-A120.

Smith, D. G., and Jol, H. M., 1992. Ground-penetrating radar investigation of a Lake Bonneville delta, Provo level, Brigham City, Utah, *Geology*, **20**, 1083-1086.

Soar, P. J., and Thorne, C. R., 2001. *Channel restoration design for meandering rivers*, U.S. Army Engineer Research and Development Center, Vicksburg, Miss.

Spillmann, T., Maurer, H., Willenberg, H., Evans, K. F., Heincke, B., and Green, A. G., 2007. Characterization of an unstable rock mass based on borehole logs and diverse borehole radar data, *Journal of Applied Geophysics*, **61**, 16-38.

Springer, R. K., and Gelhar, L. W., 1991. Characterization of large-scale aquifer heterogeneity in glacial outwash by analysis of slug tests with oscillatory response, *US Geological Survey, Cape Cod*, Report 91-4034.

Stanford, J. A., and Ward, J. V., 1988. The hyporheic habitat of river ecosystems, *Nature*, **335**, 64-66.

Stanford, J. A., and Ward, J. V., 1993. An ecosystem perspective of alluvial rivers - connectivity and the hyporheic corridor, *Journal of the North American Benthological Society*, **12**, 48-60.

Stauffer, F., and Dracos, T., 1986. Experimental and numerical study of water and solute infiltration in layered porous-media, *Journal of Hydrology*, **84**, 9-34.

Storey, R. G., Howard, K. W. F., and Williams, D. D., 2003. Factors controlling riffle-scale hyporheic exchange flows and their seasonal changes in a gaining stream: A three-dimensional groundwater flow model, *Water Resources Research*, **39**, 1034.

Streich, R., van der Kruk, J., and Green, A. G., 2006. Three-dimensional multicomponent georadar imaging of sedimentary structures, *Near Surface Geophysics*, **4**, 39-48.

Streich, R., and van der Kruk, J., 2007a. Accurate imaging of multicomponent GPR data based on exact radiation patterns, *Ieee Transactions on Geoscience and Remote Sensing*, **45**, 93-103.

Streich, R., and van der Kruk, J., 2007b. Characterizing a GPR antenna system by near-field electric field measurements, *Geophysics*, **72**, A51-A55.

Stummer, P., Maurer, H., and Green, A. G., 2004. Experimental design: Electrical resistivity data sets that provide optimum subsurface information, *Geophysics*, **69**, 120-139.

Suski, B., Revil, A., Titov, K., Konosavsky, P., Voltz, M., et al., 2006. Monitoring of an infiltration experiment using the self-potential method, *Water Resources Research*, **42**, W08418.

SVGW, 2004. Jahrbuch 2003/2004, *SVGW, Zürich*.

SVGW, 2007. Empfehlungen – Revitalisierung im Einflussbereich von Trinkwasserfassungen, *Zürich, Switzerland*.

Talley, J., Baker, G. S., Becker, M. W., and Beyrle, N., 2005. Four dimensional mapping of tracer channelization in subhorizontal bedrock fractures using surface ground penetrating radar, *Geophysical Research Letters*, **32**, L04401.

Tarantola, A., 1984a. Inversion of seismic-reflection data in the acoustic approximation, *Geophysics*, **49**, 1259-1266.

Tarantola, A., 1984b. Linearized inversion of seismic-reflection data, *Geophysical Prospecting*, **32**, 998-1015.

Tarantola, A., 1986. A strategy for nonlinear elastic inversion of seismic-reflection data, *Geophysics*, **51**, 1893-1903.

Thony, J. L., Morat, P., Vachaud, G., and LeMouel, J. L., 1997. Field characterization of the relationship between electrical potential gradients and soil water flux, *Comptes Rendus De L'Academie Des Sciences*, **325**, 317-321.

Topp, G. C., Davis, J. L., and Annan, A. P., 1980. Electromagnetic determination of soil-water content - Measurements in coaxial transmission-lines, *Water Resources Research*, **16**, 574-582.

Topp, G. C., Davis, J. L., and Annan, A. P., 1982. Electromagnetic determination of soil-water content using TDR 2. Evaluation of installation and configuration of parallel transmission-lines, *Soil Science Society of America Journal*, **46**, 678-684.

Torrence, C., and Compo, G. P., 1998. A practical guide to wavelet analysis, *Bulletin of the American Meteorological Society*, **79**, 61-78.

Touchard, F., 1999. *Caractérisation hydrogéologique d'un aquifère en socle fracture. Site de Ploëmeur (Morbihan)*: PhD thesis, University of Rennes I.

Trefry, M. G., and Muffels, C., 2007. Feflow: A finite-element ground water flow and transport modeling tool, *Ground Water*, **45**, 525-528.

Triska, F. J., Kennedy, V. C., Avanzino, R. J., Zellweger, G. W., and Bencala, K. E., 1989. Retention and transport of nutrients in a 3rd-order stream in Northwestern California - hyporheic processes, *Ecology*, **70**, 1893-1905.

Triska, F. J., Duff, J. H., and Avanzino, R. J., 1993a. Patterns of hydrological exchange and nutrient transformation in the hyporheic zone of a gravel-bottom stream - examining terrestrial aquatic linkages, *Freshwater Biology*, **29**, 259-274.

Triska, F. J., Duff, J. H., and Avanzino, R. J., 1993b. The role of water exchange between a stream channel and its hyporheic zone in nitrogen cycling at the terrestrial aquatic interface, *Hydrobiologia*, **251**, 167-184.

Tronicke, J., Dietrich, P., Wahlig, U., and Appel, E., 2002. Integrating surface georadar and crosshole radar tomography: A validation experiment in braided stream deposits, *Geophysics*, **67**, 1516-1523.

Tronicke, J., and Holliger, K., 2004. Effects of gas- and water-filled boreholes on the amplitudes of crosshole georadar data as inferred from experimental evidence, *Geophysics*, **69**, 1255-1260.

Tronicke, J., Holliger, K., Barrash, W., and Knoll, M. D., 2004. Multivariate analysis of cross-hole georadar velocity and attenuation tomograms for aquifer zonation, *Water Resources Research*, **40**, W01519.

Trubilowicz, J., Cai, K., and Weiler, M., 2009. Viability of motes for hydrological measurement, *Water Resources Research*, **45**, W00D22.

Trush, W. J., McBain, S. M., and Leopold, L. B., 2000. Attributes of an alluvial river and their relation to water policy and management, *Proceedings of the National Academy of Sciences of the United States of America*, **97**, 11858-11863.

Tryggvason, A., Rögnvaldsson, S. T., and Flóvenz, Ó. G., 2002. Three-dimensional imaging of the P- and S-wave velocity structure and earthquake locations beneath Southwest Iceland, *Geophysical Journal International*, **151**, 848-866.

Tryggvason, A., and Linde, N., 2006. Local earthquake (LE) tomography with joint inversion for P- and S-wave velocities using structural constraints, *Geophysical Research Letters*, **33**, L07303.

Tryggvason, A., and Bergman, B., 2006. A traveltime reciprocity discrepancy in the Podvin & Lecomte time3d finite difference algorithm, *Geophysical Journal International*, **165**, 432-435.

Tsoflias, G. P., Halihan, T., and Sharp, J. M., 2001. Monitoring pumping test response in a fractured aquifer using ground-penetrating radar, *Water Resources Research*, **37**, 1221-1229.

Tsoflias, G. P., and Becker, M. W., 2008. Ground-penetrating-radar response to fracture-fluid salinity: Why lower frequencies are favorable for resolving salinity changes, *Geophysics*, **73**, J25-J30.

Tubino, M., and Seminara, G., 1990. Free forced interactions in developing meanders and suppression of free bars, *Journal of Fluid Mechanics*, **214**, 131-159.

Tufenkji, N., Ryan, J. N., and Elimelech, M., 2002. The promise of bank filtration, *Environmental Science & Technology*, **36**, 422A-428A.

Turesson, A., 2006. Water content and porosity estimated from ground-penetrating radar and resistivity, *Journal of Applied Geophysics*, **58**, 99-111.

van Genuchten, M. T., 1980. A closed-form equation for predicting the hydraulic conductivity of unsaturated soils, *Soil Science Society of America Journal*, **44**, 892-898.

Vasco, D. W., Peterson, J. E., and Majer, E. L., 1995. Beyond ray tomography - Wavepaths and fresnel volumes, *Geophysics*, **60**, 1790-1804.

Vereecken, H., Binley, A., Cassiani, G., Revil, A., and Titov, K. (Eds.), 2006. *Applied hydrogeophysics*, Springer, Dordrecht, The Netherlands.

Vereecken, H., Huisman, J. A., Bogena, H., Vanderborght, J., Vrugt, J. A., and Hopmans, J. W., 2008. On the value of soil moisture measurements in vadose zone hydrology: A review, *Water Resources Research*, **44**, W00D06.

Vogt, T., Hoehn, E., Schneider, P., and Cirpka, O. A., 2009. Untersuchung der Flusswasserinfiltration in voralpinen Schottern mittels Zeitreihenanalyse, *Grundwasser*, **14**, 179-194.

Vogt, T., Schneider, P., Hahn-Woernle, L., and Cirpka, O. A., 2010a. Estimation of seepage rates in a losing stream by means of fiber-optic high-resolution vertical temperature profiling, *Journal of Hydrology*, **380**, 154-164.

Vogt, T., Hoehn, E., Schneider, P., Freund, A., Schirmer, M., and Cirpka, O. A., 2010b. Fluctuations of electrical conductivity as a natural tracer for bank filtration in a losing stream, *Advances in Water Resources*, **33**, 1296-1308.

von Gunten, H. R., Karametaxas, G., and Keil, R., 1994. Chemical Processes in Infiltrated Riverbed Sediments, *Environmental Science & Technology*, **28**, 2087-2093.

von Gunten, U., and Zobrist, J., 1993. Biogeochemical changes in groundwater-infiltration systems - column studies, *Geochimica Et Cosmochimica Acta*, **57**, 3895-3906.

Vozoff, K., and Jupp, D. L. B., 1975. Joint inversion of geophysical data, *Geophysical Journal of the Royal Astronomical Society*, **42**, 977-991.

Ward, A. S., Gooseff, M. N., and Singha, K., 2010. Imaging hyporheic zone solute transport using electrical resistivity, *Hydrological Processes*, **24**, 948-953.

Ward, J. V., 1989. The four-dimensional nature of lotic ecosystems, *Journal of the North American Benthological Society*, **8**, 2-8.

Watanabe, T., Nihei, K. T., Nakagawa, S., and Myer, L. R., 2004. Viscoacoustic wave form inversion of transmission data for velocity and attenuation, *Journal of the Acoustical Society of America*, **115**, 3059-3067.

Waxman, M. H., and Smits, L. J. M., 1968. Electrical Conductivities in Oil-Bearing Shaly Sands, *Society of Petroleum Engineers Journal*, **8**, 107.

West, L. J., Handley, K., Huang, Y., and Pokar, M., 2003. Radar frequency dielectric dispersion in sandstone: Implications for determination of moisture and clay content, *Water Resources Research*, **39**, 1026.

Western, A. W., Grayson, R. B., and Blöschl, G., 2002. Scaling of soil moisture: A hydrologic perspective, *Annual Review of Earth and Planetary Sciences*, **30**, 149-180.

Wilkinson, P. B., Meldrum, P. I., Kuras, O., Chambers, J. E., Holyoake, S. J., and Ogilvy, R. D., 2010. High-resolution electrical resistivity tomography monitoring of a tracer test in a confined aquifer, *Journal of Applied Geophysics*, **70**, 268-276.

Winship, P., Binley, A., and Gomez, D., 2006. Flow and transport in the unsaturated Sherwood Sandstone: Characterization using cross-borehole geophysical methods, *Fluid Flow and Solute Movement in Sandstones: The Onshore UK Permo-Triassic Red Bed Sequence*, **263**, 219-231.

Wishart, D. N., Slater, L. D., and Gates, A. E., 2006. Self potential improves characterization of hydraulically-active fractures from azimuthal geoelectrical measurements, *Geophysical Research Letters*, **33**, L17314.

Woessner, W. W., 2000. Stream and fluvial plain ground water interactions: Rescaling hydrogeologic thought, *Ground Water*, **38**, 423-429.

Wombacher, A., and Schneider, P., 2010. Observation centric sensor data model, *Technical Report TR-CTIT-10-13, University of Twente, Enschede*, ISSN 1381-3625.

Woolsey, S., Capelli, F., Gonser, T., Hoehn, E., Hostmann, M., et al., 2007. A strategy to assess river restoration success, *Freshwater Biology*, **52**, 752-769.

Worthington, P. F., 1993. The uses and abuses of the archie equations 1. The formation factor porosity relationship, *Journal of Applied Geophysics*, **30**, 215-228.

Wriedt, G., and Rode, M., 2006. Modelling nitrate transport and turnover in a lowland catchment system, *Journal of Hydrology*, **328**, 157-176.

Wroblicky, G. J., Campana, M. E., Valett, H. M., and Dahm, C. N., 1998. Seasonal variation in surface-subsurface water exchange and lateral hyporheic area of two stream-aquifer systems, *Water Resources Research*, **34**, 317-328.

Yeh, T. C. J., Liu, S., Glass, R. J., Baker, K., Brainard, J. R., et al., 2002. A geostatistically based inverse model for electrical resistivity surveys and its applications to vadose zone hydrology, *Water Resources Research*, **38**, 1278.

Yeh, T. C. J., Lee, C. H., Hsu, K. C., Illman, W. A., Barrash, W., et al., 2008. A view toward the future of subsurface characterization: CAT scanning groundwater basins, *Water Resources Research*, **44**, W03301.

Yilmaz, Ö., 2001. *Seismic data processing*, Society of Exploration Geophysicists, Tulsa, USA.

Zhang, J., and Morgan, F. D., 1997. Joint Seismic and Electrical Tomography, *Proceedings of the Symposium on the Application of Geophysics to Engineering and Environmental Problems*, 391-396.

Zhdanov, M. S., 2009. New advances in regularized inversion of gravity and electromagnetic data, *Geophysical Prospecting*, **57**, 463-478.

Zhou, B., and Greenhalgh, S. A., 2003. Crosshole seismic inversion with normalized full-waveform amplitude data, *Geophysics*, **68**, 1320-1330.

Zonge, K., Wynn, J., and Urquhart, S., 2005. Resistivity, induced polarization, and complex resistivity, in *Near Surface Geophysics*, edited by D. K. Butler, pp. 265-300, SEG.

Zurbuchen, B. R., Zlotnik, V. A., and Butler, J. J., 2002. Dynamic interpretation of slug tests in highly permeable aquifers, *Water Resources Research*, **38**, 1025.